

THE (BLACK HOLE MASS)—(COLOR) RELATIONS FOR EARLY- AND LATE-TYPE GALAXIES: RED AND BLUE SEQUENCES

BILLIGN T. DULLO¹, ALEXANDRE Y. K. BOUQUIN^{1,2,3}, ARMANDO GIL DE PAZ¹, JOHAN H. KNAPEN^{2,3}, AND JAVIER GORGAS¹

¹ Departamento de Física de la Tierra y Astrofísica, Instituto de Física de Partículas y del Cosmos IPARCOS, Universidad Complutense de Madrid, E-28040 Madrid, Spain

² Instituto de Astrofísica de Canarias, Vía Láctea S/N, E-38205 La Laguna, Spain and

³ Departamento de Astrofísica, Universidad de La Laguna, E-38206 La Laguna, Spain

Draft version June 19, 2020

ABSTRACT

Tight correlations between supermassive black hole (SMBH) mass (M_{BH}) and the properties of the host galaxy have useful implications for our understanding of the growth of SMBHs and evolution of galaxies. Here, we present newly observed correlations between M_{BH} and the host galaxy total UV— [3.6] color ($\mathcal{C}_{\text{UV,tot}}$, Pearson’s $r = 0.6 - 0.7$) for a sample of 67 galaxies (20 early-type galaxies and 47 late-type galaxies) with directly measured M_{BH} in the *GALEX*/*S*⁴*G* survey. The colors are carefully measured in a homogeneous manner using the galaxies’ FUV, NUV and 3.6 μm magnitudes and their multi-component structural decompositions in the literature. We find that more massive SMBHs are hosted by (early- and late-type) galaxies with redder colors, but the $M_{\text{BH}} - \mathcal{C}_{\text{UV,tot}}$ relations for the two morphological types have slopes that differ at $\sim 2\sigma$ level. Early-type galaxies define a red sequence in the $M_{\text{BH}} - \mathcal{C}_{\text{UV,tot}}$ diagrams, while late-type galaxies trace a blue sequence. Within the assumption that the specific star formation rate of a galaxy (sSFR) is well traced by $L_{\text{UV}}/L_{3.6}$, it follows that the SMBH masses for late-type galaxies exhibit a steeper dependence on sSFR than those for early-type galaxies. The $M_{\text{BH}} - \mathcal{C}_{\text{UV,tot}}$ and $M_{\text{BH}} - L_{3.6,\text{tot}}$ relations for the sample galaxies reveal a comparable level of vertical scatter in the $\log M_{\text{BH}}$ direction, roughly 5% – 27% more than the vertical scatter of the $M_{\text{BH}} - \sigma$ relation. Our $M_{\text{BH}} - \mathcal{C}_{\text{UV,tot}}$ relations suggest different channels of SMBH growth for early- and late-type galaxies, consistent with their distinct formation and evolution scenarios. These new relations offer the prospect of estimating SMBH masses reliably using only the galaxy color. Furthermore, we show that they are capable of estimating intermediate black hole masses in low-mass, early- and late-type galaxies.

Subject headings: galaxies: elliptical and lenticular, cD — galaxies: fundamental parameter — galaxies: nuclei — galaxies: photometry — galaxies: structure

1. INTRODUCTION

Almost all local galaxies are believed to harbor a supermassive black hole (SMBH, $M_{\text{BH}} \sim 10^5 - 10^9 M_{\odot}$) at their center (Magorrian et al. 1998; Richstone et al. 1998; Ferrarese & Ford 2005). The connection between SMBHs and their host galaxies has been a subject of interest, since Kormendy & Richstone (1995, see also Dressler 1989) first reported a linear correlation between SMBH mass (M_{BH}) and the luminosity of the host bulge (i.e., the entire galaxy in case of elliptical galaxies), see Kormendy & Ho (2013); Graham (2016) for recent reviews. SMBH masses scale with a number of host galaxy properties including stellar velocity dispersion (σ , Ferrarese & Merritt 2000; Gebhardt et al. 2000), bulge luminosity (L_{bulge}) and bulge mass (M_{bulge} , Kormendy & Richstone 1995; Magorrian et al. 1998), depleted stellar core (e.g., Dullo 2019) and stellar concentration (Graham et al. 2001). Not only did these scaling relations allow us to predict M_{BH} in galaxies, but they also led to a suggestion that the fueling and growth rate of the central SMBH are intimately coupled to the star formation rate and stellar mass build-up of the host galaxy. However, the exact nature of the physical mechanism driving this connection remains unclear.

Accretion of gas onto SMBHs triggers active galactic

nucleus (AGN) feedback, critical for the regulation of the star formation and growth of the host galaxy (e.g., Silk & Rees 1998; Fabian 1999; Springel et al. 2005; Di Matteo et al. 2005; Croton et al. 2006; Hopkins et al. 2006). The distinct formation histories, colors and structural properties of early- and late-type galaxies may therefore reflect two different channels of gas accretion and SMBH growth for the two morphological types (see Hopkins & Hernquist 2009; Shankar et al. 2009; Schawinski et al. 2010, 2014; Krajnović et al. 2018). Observations show that early-type (i.e., lenticular and elliptical) galaxies do not correlate with SMBHs in the same manner as late-type (i.e., spiral) galaxies do (e.g., McConnell & Ma 2013; Saglia et al. 2016; Krajnović et al. 2018; Sahu et al. 2019). Early-type galaxies are typically red with low level star-formation rate, while late-type galaxies have blue colors and are actively star forming. This dichotomy gives rise to a bimodal distribution of galaxies in the color-magnitude diagram—early-type galaxies define a red-sequence separate from late-type galaxies which reside in a blue cloud (e.g., Chester & Roberts 1964; Visvanathan & Griersmith 1977; Baldry et al. 2004; Brammer et al. 2009).

In the hierarchical galaxy formation scenario, early-type galaxies are built through mergers of smaller

systems and accretion events (e.g., White & Rees 1978; Naab et al. 2006b; Hopkins et al. 2009a,b; Rodriguez-Gomez et al. 2016; Mundy et al. 2017). Major merger driven inflow of gas into the nuclear regions of the newly formed merger remnant can produce rapid bursts of star formation and fuel the SMBH (Barnes & Hernquist 1991, 1996; Naab et al. 2006a; Hopkins & Quataert 2010). For late-type (i.e., spiral) galaxies, one of the most advocated formation scenarios is secular evolution involving non-axisymmetric stellar structures, such as bars and spiral arms which can drive an inflow of gas from the disk into the nuclear region and onto the central SMBH (Kormendy 1982; Courteau et al. 1996; Carollo et al. 1997; Kormendy & Kennicutt 2004; Athanassoula 2005; Laurikainen et al. 2007; Fisher & Drory 2008; Graham & Worley 2008; Gadotti 2009; Tonini et al. 2016; Dullo et al. 2016, 2019).

A related issue is the observed departures from single power-law relations (e.g., bends and offsets) in SMBH scaling diagrams at the low-mass and high-mass ends or when the galaxy sample contains Sérsic and core-Sérsic galaxies. In particular, Graham (2012, see also Graham & Scott 2013) reported two separate $M_{\text{BH}} - L_{\text{bulge}}$ relations with distinct slopes for Sérsic and core-Sérsic galaxies. Core-Sérsic galaxies are luminous ($M_B \lesssim -20.5 \pm 0.5$ mag) galaxies which exhibit a flattening in their inner stellar light distribution due to a central deficit of light relative to the inward extrapolation of their outer Sérsic (1968) light profile (Faber et al. 1997; Graham et al. 2003; Hopkins et al. 2009b; Dullo & Graham 2012, 2013, 2014, 2015; Dullo et al. 2017, 2018; Dullo 2019). They are thought to have formed from a few number of gas-poor major merger events¹, but a small fraction of them can host molecular gas reservoirs that feeds an ongoing, low level star formation (Davis et al. 2019). In contrast, the low- and intermediate luminosity ($M_B \gtrsim -20.5$ mag) Sérsic galaxies, with no depleted cores, are product of gas-rich mergers (Hopkins et al. 2009a; Dullo & Graham 2012, 2014; Dullo et al. 2016, 2019). Departures from the best-fitting single power-law relation in a BH scaling diagram may hold implications for SMBH and galaxy co-evolution, however, as the majority of SMBH scaling relations to date are based on host galaxy properties that trace solely the old stellar populations, disregarding the young and intermediate-aged stars, the exact mechanism establishing the supposed coupling between the growth of the SMBHs and the build-up of their host galaxies is unclear.

Here, we explore a scenario in which the complex interplay between the details of the SMBH growth, efficiency of AGN feedback, regulated star formation histories and major merger histories of the host galaxy establish a relation between the SMBH and color of the host galaxy (see also Schawinski et al. 2010, 2014). There are emerging evidences showing a link between M_{BH} and the star formation rate in nearby galaxies. Terrazas et al. (2017) reported an inverse correlation between specific star formation rate (sSFR) and specific supermassive black hole

mass. Martín-Navarro et al. (2018) observed a trend between SMBH mass and host galaxy star formation histories, where the star formation in galaxies hosting more massive SMBHs was quenched early and more efficiently than in those with less massive SMBHs (see also van Son et al. 2019). Given the UV–[3.6] color (C_{UV}) is a good proxy for sSFR (e.g., Bouquin et al. 2018), a correlation between M_{BH} and UV–[3.6] color is expected. The UV flux is a proxy for the current star formation rate since it traces massive, young stars. The emission at $3.6 \mu\text{m}$, which is less affected by dust extinction, is a good proxy for stellar mass since it traces primarily older stellar populations. However, a small fraction (5%–15%) of the $3.6 \mu\text{m}$ flux can be due to contributions from intermediate-age stars, polycyclic aromatic hydrocarbons and hot dust (Meidt et al. 2012). Hitherto, the $M_{\text{BH}} - \text{color}$ relation was overlooked, in part, owing to the narrow wavelength baselines commonly used to determine colors.

In this paper, we present (for the first time) correlations between M_{BH} and C_{UV} colors for 67 *GALEX*/S⁴G galaxies with directly measured SMBH masses (van den Bosch 2016) and homogeneously determined *GALEX* FUV and NUV, and *Spitzer* $3.6 \mu\text{m}$ magnitudes (Bouquin et al. 2018). Dividing the sample galaxies by morphology, we fit two different $M_{\text{BH}} - C_{\text{UV}}$ relations with distinct slopes for early- and late-type galaxies.

The $M_{\text{BH}} - C_{\text{UV}}$ relation has multiple, important applications. It allows the SMBHs in early- and late-type galaxies to be predicted free from uncertainties due to distances and mass-to-light ratios, although there are uncertainties due to K-corrections for more distant galaxies. Furthermore, using $M_{\text{BH}} - C_{\text{UV}}$ relation we hope to understand properly the poorly constrained low-mass end of the SMBH scaling relations. In so doing, we can predict SMBHs or intermediate-mass black holes (IMBHs) with masses $\sim 100 - 10^5 M_{\odot}$ in low-mass systems and bulgeless spiral galaxies. In addition, since colors are easy to measure even for high-redshift galaxies, studying the galaxy color and BH mass evolution at different epochs may provide further clues on the different channels of BH growth.

The paper is organized as follows. Section 2.1 describes the sample selection. Sections 2.2 and 2.3 describe the SMBH data, and the UV and $3.6 \mu\text{m}$ apparent, asymptotic magnitudes. The derivation of bulge, disk and total magnitudes for the sample galaxies along with the corresponding dust corrections and error measurements are discussed in Sections 3.1 and 3.2, respectively. We go on to discuss the regression techniques employed for fitting the BH scaling relations in Section 3.3 and present the results from our regression analyses in Sections 3.4 and 3.5. Section 4 provides a discussion of our results, including the origin and implications of the $M_{\text{BH}} - C_{\text{UV}}$ relations. Section 5 summarizes our main conclusions.

There are four appendices at the end of this paper (Appendices A, B, C and D). Appendix A discusses our implementation of the MCMC Bayesian statistical method. Notes on five notable outliers in the $M_{\text{BH}} - C_{\text{UV}}$ relations are given in Appendix B. Appendix C includes a table, listing apparent total magnitudes, flux ratios, dust corrections and direct SMBH masses for our sample galax-

¹ The depleted cores of core-Sérsic galaxies are thought to be scoured by coalescing binary SMBHs formed in the gas-poor merger events (Begelman et al. 1980; Ebisuzaki et al. 1991; Merritt 2006).

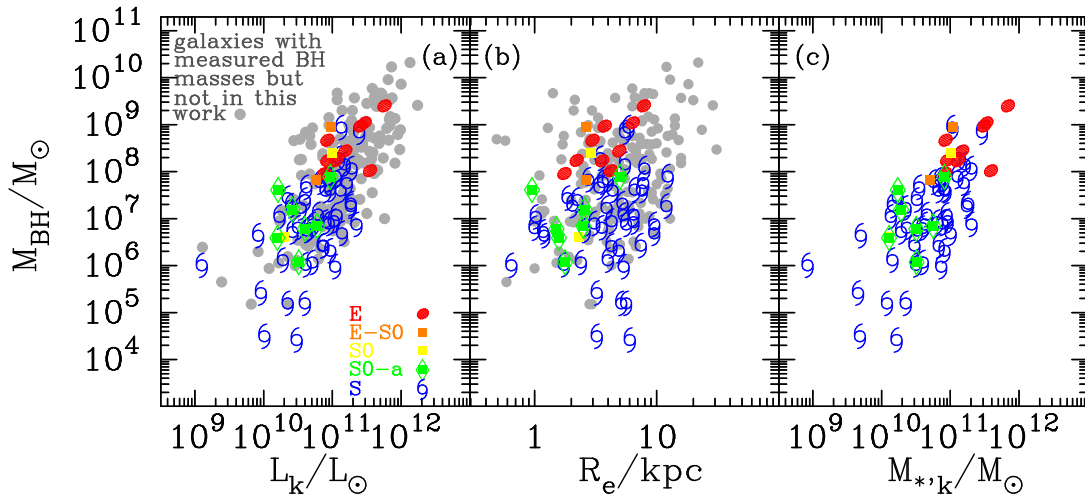


FIG. 1.— Galaxies with measured SMBH masses (M_{BH}). M_{BH} plotted as a function of (a) total K_s -band luminosity and (b) the half-light radius (R_e) for a sample of 245 galaxies with measured M_{BH} (van den Bosch 2016, his Table 2). Colored symbols denote our sample of 67 galaxies, whereas filled gray circles show the remaining 178 galaxies with measured M_{BH} in van den Bosch (2016, his Table 2). Panel (c): M_{BH} versus total K_s -band stellar mass ($M_{*,k}$) for our sample derived from the total K_s -band luminosities assuming the K_s -band mass-to-light ratio $M_*/L_k = 0.10\sigma^{0.45}$ (van den Bosch 2016). Morphological classifications are from HyperLEDA.

ies. We tentatively predict BH masses in a sample of 1382 *GALEX*/*S*⁴*G* galaxies with no measured BH masses using our $M_{\text{BH}} - C_{\text{UV}}$ relations and tabulated them in Appendix D.

2. SAMPLE AND DATA

2.1. Sample Selection

Our investigation of correlations between the SMBH mass (M_{BH}) and $(\text{UV} - [3.6])$ galaxy color uses UV and $3.6 \mu\text{m}$ magnitudes, determined in a homogeneous manner, for a large sample of galaxies with measured SMBH masses. Henceforth, we designate the $(\text{UV} - [3.6])$ color as C . Bouquin et al. (2015, 2018) provided far-UV (FUV, $\lambda_{\text{eff}} \sim 1526 \text{ \AA}$), near-UV (NUV, $\lambda_{\text{eff}} \sim 2267 \text{ \AA}$) and $3.6 \mu\text{m}$ asymptotic magnitudes for a sample of 1931 nearby galaxies taken from the *Spitzer* Survey of Stellar Structure in Galaxies (*S*⁴*G*) sample (Sheth et al. 2010). They used ultraviolet (UV) and near-infrared ($3.6 \mu\text{m}$) imaging data obtained with the *Galaxy Evolution Explorer*, *GALEX*, (Martin et al. 2005; Gil de Paz et al. 2007) and the Infrared Array Camera (IRAC) on the *Spitzer Space Telescope*, respectively. We use the SMBH sample presented in van den Bosch (2016, his Table 2). They publish a compilation of directly measured SMBH masses (M_{BH}), half-light radii (R_e), and total K_s -band luminosities (L_k) for a large sample of 245 galaxies. We selected all galaxies that were in common to Bouquin et al. (2018) and van den Bosch (2016), resulting in a sample of 67 galaxies studied in this paper. Homogenized mean central velocity dispersions (σ) and morphological classifications (elliptical E, elliptical-lenticular E-S0, lenticular S0, lenticular-spiral S0-a and spiral S) the sample galaxies were obtained from HyperLEDA² (Paturel et al. 2003; Makarov et al. 2014). In the analysis of the scaling relations (Tables 1, 2, 3 and 4), the galaxies are divided into two, broad morphological classes, early-type galaxies (9 Es, 2 E-S0s, 2 S0s and 7 S0-a) and late-type galaxies (47 Ss). Most of our late-type galaxies are disk dominated. The full list of galaxies

and their properties are presented in Appendix C.

In Fig. 1, we check on potential sample selection biases by comparing M_{BH} , R_e , and L_k of our sample and those of other (178) known galaxies with measured black hole masses using data from van den Bosch (2016, his Table 2). Both the early- and late-type galaxies in our sample probe large range in M_{BH} , R_e , and L_k to allow a robust investigation of the $M_{\text{BH}} - C$ relations. We also find that our early- and late-type galaxies span a wide range in stellar mass ($M_{*,k}$), Fig. 1 c. The galaxy stellar masses we compute using L_k and assuming the K_s -band mass-to-light ratio $M_*/L_k = 0.10\sigma^{0.45}$ (van den Bosch 2016). Late-type galaxies in our sample have $M_{*,k}$ that range from $10^9 M_\odot$ to $2 \times 10^{11} M_\odot$, and for 75% of them $M_{*,k}/M_\odot \gtrsim 2 \times 10^{10}$. For the early-type galaxies, $10^{10} \lesssim M_{*,k}/M_\odot \lesssim 10^{12}$, and 90% of these galaxies have $M_{*,k}/M_\odot \gtrsim 2 \times 10^{10}$. It worth noting that the *GALEX*/*S*⁴*G* sample galaxies (Bouquin et al. 2018) were chosen to have radio-derived radial velocities of $V_{\text{radio}} < 3000 \text{ Km s}^{-1}$ in HyperLEDA. As such, the sample lacks HI-poor, extremely massive galaxies including brightest cluster galaxies (BCGs).

2.2. Black hole masses

Among our selected sample of 67 galaxies, 64 have SMBH masses (M_{BH}) determined from stellar, gas or maser kinematic measurements. For the remaining 3/67 galaxies (NGC 4051, NGC 4593 and NGC 5273), M_{BH} were based on reverberation mapping (Bahcall et al. 1972; Peterson 1993). Of the 67 galaxies, 62 harbor black holes that are supermassive (i.e., $M_{\text{BH}} \gtrsim 10^6 M_\odot$); see Appendix C. While the remaining 5 sample galaxies have $2 \times 10^4 M_\odot \lesssim (M_{\text{BH}}) \lesssim 3 \times 10^9 M_\odot$, we also refer to these black holes as SMBHs. The sample includes 25 galaxies with M_{BH} upper limits, comprised of 23 late-type galaxies and 2 early-type galaxies. We discuss how the inclusion of upper limits affects the BH scaling relations in Section 3. The uncertainties on M_{BH} were taken from van den Bosch (2016).

² <http://leda.univ-lyon1.fr>

TABLE 1
 $M_{\text{BH}} - C_{\text{FUV,tot}}$ SCALING RELATIONS FOR EARLY- AND LATE-TYPE GALAXIES.

$Y = \beta X + \alpha, X = C_{\text{FUV,tot}} - 6.5, Y = \log M_{\text{BH}}$ early-type galaxies, Fig. 2, left										
Regression method	Y X		X Y		Bisector		r	Δ [dex]	ϵ [dex]	N
(1)	α	β	α	β	α	β	(8)	(9)	(10)	(11)
BCES	8.12 ± 0.18	1.28 ± 0.40	8.30 ± 0.31	2.65 ± 0.82	8.18 ± 0.20	1.75 ± 0.41	0.61	0.86	—	18
LINMIX_ERR	8.15 ± 0.22	1.25 ± 0.44	8.34 ± 0.23	2.47 ± 0.84	—	1.71 ± 0.51	—	—	0.69 ± 0.20	18
OLS	8.10 ± 0.17	1.04 ± 0.30	8.32 ± 0.27	2.59 ± 0.77	8.17 ± 0.18	1.57 ± 0.27	—	0.87	—	18
MCMC	—	—	—	—	Symmetric 8.27 ± 0.25 2.06 ± 0.63		—	0.85	—	18
$Y = \beta X + \alpha, X = C_{\text{FUV,tot}} - 3.3, Y = \log M_{\text{BH}}$ late-type galaxies, Fig. 2, left										
Regression method	Y X		X Y		Bisector		r	Δ [dex]	ϵ [dex]	N
(1)	α	β	α	β	α	β	(8)	(9)	(10)	(11)
BCES	7.01 ± 0.13	0.82 ± 0.20	7.06 ± 0.19	1.35 ± 0.36	7.03 ± 0.14	1.03 ± 0.13	0.60	0.87	—	45
LINMIX_ERR	7.07 ± 0.13	0.87 ± 0.26	7.09 ± 0.13	1.59 ± 0.38	—	1.17 ± 0.27	—	—	0.69 ± 0.22	45
OLS	6.97 ± 0.12	0.62 ± 0.16	7.10 ± 0.22	1.82 ± 0.36	7.02 ± 0.14	1.05 ± 0.12	—	0.87	—	45
MCMC	—	—	—	—	Symmetric 6.95 ± 0.11 0.87 ± 0.17		—	0.81	—	45
$Y = \beta X + \alpha, X = C_{\text{NUV,tot}} - 5.0, Y = \log M_{\text{BH}}$ early-type galaxies, Fig. 2, right										
Regression method	Y X		X Y		Bisector		r	Δ [dex]	ϵ [dex]	N
(1)	α	β	α	β	α	β	(8)	(9)	(10)	(11)
BCES	8.07 ± 0.15	1.57 ± 0.36	8.21 ± 0.29	2.74 ± 0.99	8.12 ± 0.17	1.95 ± 0.28	0.70	0.72	—	19
LINMIX_ERR	8.10 ± 0.20	1.66 ± 0.55	8.19 ± 0.20	2.63 ± 0.79	—	2.04 ± 0.60	—	—	0.66 ± 0.18	19
OLS	8.06 ± 0.15	1.27 ± 0.28	8.18 ± 0.24	2.65 ± 0.68	8.11 ± 0.16	1.76 ± 0.20	—	0.68	—	19
MCMC	—	—	—	—	Symmetric 8.06 ± 0.26 2.33 ± 0.74		—	0.82	—	19
$Y = \beta X + \alpha, X = C_{\text{NUV,tot}} - 2.7, Y = \log M_{\text{BH}}$ late-type galaxies, Fig. 2, right										
Regression method	Y X		X Y		Bisector		r	Δ [dex]	ϵ [dex]	N
(1)	α	β	α	β	α	β	(8)	(9)	(10)	(11)
BCES	6.96 ± 0.15	1.24 ± 0.35	6.96 ± 0.17	1.61 ± 0.33	6.96 ± 0.15	1.38 ± 0.23	0.65	0.86	—	45
LINMIX_ERR	7.02 ± 0.12	1.08 ± 0.30	8.32 ± 0.27	1.86 ± 0.41	—	—	—	—	0.66 ± 0.18	45
OLS	6.94 ± 0.12	0.82 ± 0.17	6.94 ± 0.18	1.94 ± 0.35	6.94 ± 0.13	1.24 ± 0.13	—	0.83	—	45
MCMC	—	—	—	—	Symmetric 6.90 ± 0.13 1.35 ± 0.26		—	0.85	—	45

Notes.— Correlation between SMBH mass (M_{BH}) and total UV - [3.6] color ($C_{\text{UV,tot}}$) for our early- and late-type galaxies with directly measured M_{BH} . $C_{\text{FUV,tot}} = m_{\text{FUV}} - m_{3.6 \mu\text{m}}$, $C_{\text{NUV,tot}} = m_{\text{NUV}} - m_{3.6 \mu\text{m}}$, where m_{FUV} , m_{NUV} and $m_{3.6 \mu\text{m}}$ are the FUV, NUV and $3.6 \mu\text{m}$ total apparent magnitudes of the galaxies (Table 5). Col. (1) regression method. Cols. (2) and (3) are the intercepts (α) and slopes (β) from the (Y|X) regressions. Cols. (4) and (5) are α and β obtained from the (Y|X) regression fits, while cols. (6) and (7) show α and β from the symmetrical bisector regressions. The preferred slopes and intercepts are highlighted in bold. Cols. (8) Pearson correlation coefficient (r). Cols. (9) the root-mean-square (rms) scatter around the fitted BCES bisector relation in the log M_{BH} direction (Δ). Col. (10) intrinsic scatter (ϵ), see the text for details. Col. (11) number of data points contributing to the regression fits.

2.3. UV and 3.6 μm apparent asymptotic magnitudes

Bouquin et al. (2015, 2018) used the 3.6 μm surface brightness profiles from Muñoz-Mateos et al. (2015) to determine the 3.6 μm magnitudes for their galaxies. They extracted the UV surface brightness profiles of the galaxies following the prescription of Muñoz-Mateos et al. (2015). Briefly, the sky levels in galaxy images were first determined before the images were masked to avoid bright foreground and background objects (Bouquin et al. 2018, their section 3.1). The FUV, NUV and 3.6 μm radial surface brightness profiles were then extracted using a series of elliptical annuli with fixed ellipticity and position angle, after excluding the innermost regions, $R < 3''$, (Muñoz-Mateos et al. 2015; Bouquin et al. 2015, 2018). Each annulus has a width of $6''$ and measurements were taken up to $3 \times$ the major axis of the galaxy $D25$ elliptical isophote. To derive the FUV, NUV and 3.6 μm asymptotic magnitudes from the corresponding surface brightness profiles, Bouquin et al. (2018) extrapolated the growth curves. The UV, and 3.6 μm data reach depths of ~ 27 mag arcsec $^{-2}$ and ~ 26.5 mag arcsec $^{-2}$, respectively, allowing the growth curves to flatten out for most galaxies. The method yielded robust asymptotic magnitudes with errors that are within the FUV and NUV zero-point uncertainties of 0.05 and 0.03 AB mag (Morrissey et al. 2007).

3. RESULTS

3.1. Calculating dust-corrected total magnitudes

The FUV, NUV and 3.6 μm (total) asymptotic magnitudes of our sample were corrected for Galactic extinction by Bouquin et al. (2015, 2018) using the $E(B - V)$ reddening values taken from Schlegel et al. (1998). For the analyses in the paper, we define the total galaxy luminosity as the sum of the luminosities of the bulge and disk, excluding additional galaxy structural components such as bars and rings. The bulk of the galaxies in our sample are multi-component systems. Fractional luminosities of the individual structural components are needed to obtain accurate bulge and disk magnitudes from the total asymptotic magnitudes. We note that, from here on, the term ‘bulge’ is used when referring to both the spheroids of elliptical galaxies and the bulges of disk galaxies. Fortunately, Salo et al. (2015) performed detailed 2D multi-component decompositions of 3.6 μm images of all our galaxies into nuclear sources, bulges, disks and bars, and they presented fractional bulge and disk luminosities which we use to calculate the 3.6 μm bulge and disk magnitudes. For two galaxies (NGC 3368 and NGC 4258) with poor fits in Salo et al. (2015), the 3.6 μm fractional luminosities were taken from Savorgnan & Graham (2016). The bulge-to-disk flux ratio (B/D) of a galaxy depends on both the observed wavelength and galaxy morphological type (e.g., Möllenhoff 2004; Möllenhoff et al. 2006; Graham & Worley 2008; Kennedy et al. 2016). The UV B/T and D/T ratios tabulated in Appendix C were derived using the 3.6 μm B/D ratio together with the (extrapolation of the) B/D -passband-morphological type diagram from Möllenhoff (2004, his Fig. 5).

For the disk galaxies, we additionally applied the inclination (i) dependent, internal dust attenuation corrections from Driver et al. (2008, their equations 1 and 2

and Table 1) to determine dust-corrected bulge and disk magnitudes. Since Driver et al. (2008) did not provide 3.6 μm dust corrections, we rely on the prescription for their reddest bandpass (i.e., K) to correct the 3.6 μm magnitudes. These corrections are given by:

$$m_{\text{bulge,UV}}^{\text{corr}} = m_{\text{bulge,UV}}^{\text{obs}} - 1.10 - 0.95[1 - \cos(i)]^{2.18}, \quad (1)$$

$$m_{\text{disk,UV}}^{\text{corr}} = m_{\text{disk,UV}}^{\text{obs}} - 0.45 - 2.31[1 - \cos(i)]^{3.42}, \quad (2)$$

$$m_{\text{bulge,3.6}}^{\text{corr}} = m_{\text{bulge,3.6}}^{\text{obs}} - 0.11 - 0.79[1 - \cos(i)]^{2.77}, \quad (3)$$

$$m_{\text{disk,3.6}}^{\text{corr}} = m_{\text{disk,3.6}}^{\text{obs}} - 0.04 - 0.46[1 - \cos(i)]^{4.23}, \quad (4)$$

where $\cos(i) = b/a$, i.e., the minor-to-major axis ratios, which were computed for our galaxies from the minor and major galaxy diameters given in NED.

For each sample galaxy, we derived the dust-corrected total galaxy magnitude as

$$m_{\text{total}}^{\text{corr}} = -2.5 \log(10^{-0.4m_{\text{disk}}^{\text{corr}}} + 10^{-0.4m_{\text{bulge}}^{\text{corr}}}) \quad (5)$$

3.2. Uncertainties on magnitudes

Analyses of the (black hole)-(color) relations can be affected by uncertainties on the bulge, disk and total magnitudes (Section 3.1 and Appendix C) that are dominated by systematic errors. We account for four potential sources of systematic uncertainty. There are uncertainties on the UV and 3.6 μm asymptotic magnitudes introduced by dust contamination, imperfect sky background determination and poor masking of bright sources (Bouquin et al. 2018). For the disk galaxies, there are uncertainties due to our dust correction. There is also a need to account for uncertainties on the 3.6 μm B/T and D/T ratios (Salo et al. 2015) used to convert the asymptotic magnitudes into disk, bulge and total magnitudes. For the UV magnitudes, an additional source of systematic uncertainty is the derivation of the B/T and D/T ratios (Section 3.1). The total uncertainties associated with the UV and 3.6 μm magnitudes were calculated by adding the individual contributions in the error budget in quadrature. Appendix C lists total magnitudes and associated errors for our sample galaxies. The quoted magnitudes are in the AB system, unless noted otherwise.

3.3. Regression Analysis

Inherent differences in the employed statistical methods may systematically affect the derived BH scaling relations and it is therefore vital to explore this issue. We performed linear regression fits to $M_{\text{BH}} - \mathcal{C}$ ($= m_{\text{UV}}^{\text{corr}} - m_{3.6}^{\text{corr}}$), $M_{\text{BH}} - L_{3.6}$ and $M_{\text{BH}} - \sigma$ data using three traditional regression techniques: the Bivariate Correlated Errors and intrinsic Scatter (BCES) code (Akritas & Bershady 1996), the Bayesian linear regression routine (LINMIX_ERR, Kelly 2007) and Ordinary Least-Squares (OLS) code (Feigelson & Babu 1992), Figs. 2 and 3. The BCES routine (Akritas & Bershady 1996) was implemented in our work using the python

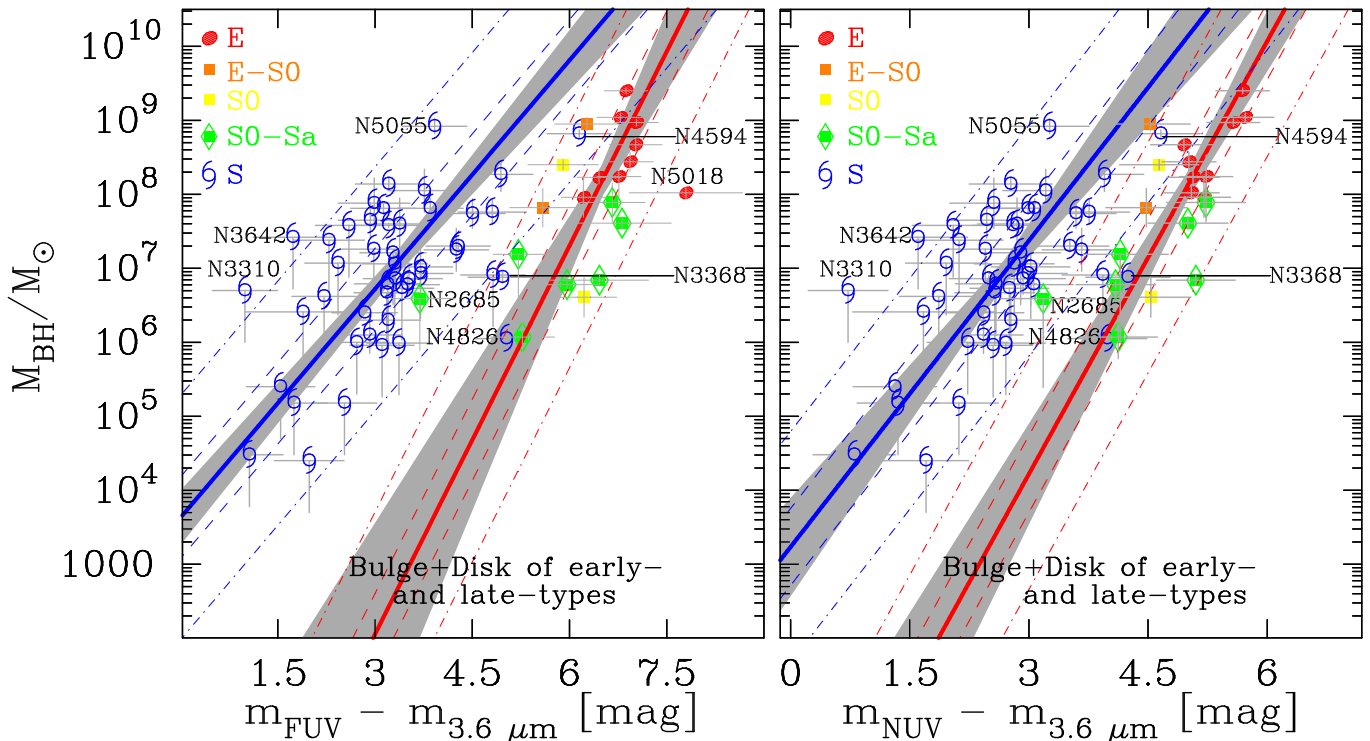


FIG. 2.— Correlations of directly measured SMBH masses (M_{BH}) with the total (i.e., bulge+disk) UV – $3.6 \mu\text{m}$ colors ($C_{\text{UV,tot}}$) of their host galaxies. $M_{\text{BH}} - C_{\text{FUV,tot}}$ relations (left) and $M_{\text{BH}} - C_{\text{NUV,tot}}$ relations (right) for early- and late-type galaxies. Our early-type morphological bin comprises E, E-S0, S0, and S0-a. Late-type galaxies (i.e., Sa, Sb, Sc, Sd, Sm and Irr) are plotted in blue. Early- and late-type galaxies, which are fit separately, define two distinct red and blue sequences with significantly different slopes (see Table 1). The solid red and solid blue lines are the symmetric BCES bisector fits to our early- and late-type data, respectively, the shaded regions cover the associated 1σ uncertainties on these fits (Table 1). The dashed and dash-dotted lines delineate the one and three times the intrinsic scatter, respectively. Errors on M_{BH} and $C_{\text{UV,tot}}$ are shown, and for galaxies with black hole upper limits we only show the lower uncertainty on M_{BH} (see the text for further detail).

module by Nemmen et al. (2012). While both the BCES and LINMIX_ERR methods take into account the intrinsic scatter and uncertainties in both M_{BH} and the host galaxy properties, only the latter can deal with ‘censored’ data, e.g., black hole mass upper limits. The OLS routine does not account for errors, we use this method to provide $M_{\text{BH}} - C$ relations independent of measurement errors.

In an effort to assess the robustness of the above linear regression fits, we have additionally performed symmetric, MCMC Bayesian linear regression fits for our (M_{BH}, C) data, which account for black hole mass upper limits (see Appendix A).

Fitting the $Y = \beta X + \alpha$ line with the BCES, LINMIX_ERR and OLS codes, we present the results from the ($Y|X$), ($X|Y$) and bisector regression analyses (Tables 1, 2 and 3). We also present the results from our symmetric, MCMC Bayesian regressions (Table 1). The ($Y|X$), ($X|Y$) regressions minimize the residuals around the fitted regression lines in the Y and X directions, respectively. The symmetrical bisector line bisects the ($Y|X$) and ($X|Y$) lines. The LINMIX_ERR code does not return bisector regressions, thus we computed the slope of line that bisects the ($Y|X$) and ($X|Y$) lines. Throughout this work, we focus on the relations from the symmetrical BCES bisector regressions (Figs. 2 and 3).

3.4. The $M_{\text{BH}} - C_{\text{UV,tot}}$ relations

In this section, we investigate the correlations between M_{BH} and total (i.e., bulge+disk) colors $C_{\text{FUV,tot}}$ ($=m_{\text{FUV,tot}}^{\text{corr}} - m_{3.6,\text{total}}^{\text{corr}}$) and $C_{\text{NUV,tot}}$ ($=m_{\text{NUV,tot}}^{\text{corr}} - m_{3.6,\text{total}}^{\text{corr}}$) for our sample of 67 galaxies comprised of 20 early-type galaxies and 47 late-type galaxies (Appendix C). In Fig. 2, we plot these correlations (Table 5), with data points color-coded based on morphological type. The regression analyses reveal that early- and late-type galaxies define two distinct red and blue sequences with markedly different slopes in the $M_{\text{BH}} - C_{\text{UV,tot}}$ diagrams, regardless of the applied regression methods (Table 1). We find that the slopes for early- and late-type galaxies are different at $\sim 2\sigma$ level (Appendix A) and the significance levels for rejecting the null hypothesis of these two morphological types having the same slope are 1.7%–6.7%. We note in passing that this trend of different slopes for early- and late-type galaxies holds for the correlations between M_{BH} and the bulge colors of the two Hubble types ($C_{\text{UV,bulge}}$, Dullo et al. in prep). For both early- and late-type galaxies, the $C_{\text{FUV,tot}}$ and M_{BH} data correlate with a Pearson correlation coefficient $r \sim 0.60$ (Table 1). The $C_{\text{NUV,tot}}$, M_{BH} data have Pearson correlation coefficients $r \sim 0.70$ and 0.65 for early- and late-type galaxies, respectively. In the $M_{\text{BH}} - C$ regression analyses, we have excluded 1 early-type galaxy (NGC 2685) and 2 late-type galaxies (NGC 3310 and NGC 4826) which offset from the relations by more than three times the intrinsic scatter

TABLE 2
 $M_{\text{BH}} - \sigma$ RELATION

Regression method	$Y=\beta X+\alpha, X=\log \sigma-2.2, Y=\log M_{\text{BH}}$ (early-type, Fig. 3, left)						r	Δ [dex]	ϵ [dex]	N
	$Y X$	$X Y$	Bisector							
(1)	α	β	α	β	α	β	(8)	(9)	(10)	(11)
BCES	7.84 ± 0.14	4.33 ± 0.80	7.81 ± 0.23	7.10 ± 1.58	7.84 ± 0.16	5.42 ± 0.90	0.72	0.67	0.70 ± 0.16	20
Regression method	$Y=\beta X+\alpha, X=\log \sigma-2.0, Y=\log M_{\text{BH}}$ (late-type, Fig. 3, left)						r	Δ [dex]	ϵ [dex]	N
	$Y X$	$X Y$	Bisector							
(1)	α	β	α	β	α	β	(8)	(9)	(10)	(11)
BCES	6.98 ± 0.10	4.00 ± 0.53	7.00 ± 0.11	5.00 ± 0.99	6.98 ± 0.10	4.49 ± 0.48	0.75	0.70	0.63 ± 0.10	45
Regression method	$Y=\beta X+\alpha, X=\log \sigma-2.0, Y=\log M_{\text{BH}}$ (all galaxies, Fig. 3, left)						r	Δ [dex]	ϵ [dex]	N
	$Y X$	$X Y$	Bisector							
(1)	α	β	α	β	α	β	(8)	(9)	(10)	(11)
BCES	6.99 ± 0.09	4.23 ± 0.40	6.92 ± 0.10	5.39 ± 0.72	6.96 ± 0.09	4.65 ± 0.35	0.78	0.68	0.62 ± 0.07	65

 Notes.— Similar to Table 1, but here showing linear regression analyses of the correlation between SMBH mass (M_{BH}) and velocity dispersion (σ).

 TABLE 3
 $M_{\text{BH}} - L_{3.6,\text{tot}}$ RELATION

Regression method	$Y=\beta X+\alpha, X=M_{3.6,\text{tot}}+18.5, Y=\log M_{\text{BH}}$ (all galaxies, Fig. 3, right)						r	Δ [dex]	ϵ [dex]	N
	$Y X$	$X Y$	Bisector							
(1)	α	β	α	β	α	β	(8)	(9)	(10)	(11)
BCES	6.96 ± 0.11	-0.37 ± 0.06	6.80 ± 0.17	-0.65 ± 0.12	6.88 ± 0.12	-0.49 ± 0.06	-0.66	0.84	0.69 ± 0.09	67

 Notes.— Similar to Table 1, but here showing linear regression analyses of the correlation between the SMBH masses (M_{BH}) and 3.6 μm total absolute magnitude of the galaxies ($M_{3.6,\text{tot}}$), see the text for details.

(Fig. 2). The early-type galaxy NGC 5018 was also excluded from the $M_{\text{BH}} - C_{\text{FUV}}$ relations, resulting in 18 early-type galaxies. Interestingly, all these four outliers are have peculiar characteristics that are discussed in Appendix B.1.

Symmetrical BCES bisector fits to the $(M_{\text{BH}}, C_{\text{FUV,tot}})$ and $(M_{\text{BH}}, C_{\text{NUV,tot}})$ data yield relations for early-type galaxies with slopes of 1.75 ± 0.41 and 1.95 ± 0.28 , respectively (Table 1), such that $M_{\text{BH}} \propto (L_{\text{FUV,tot}}/L_{3.6,\text{tot}})^{-4.38 \pm 1.03}$ and $M_{\text{BH}} \propto (L_{\text{NUV,tot}}/L_{3.6,\text{tot}})^{-4.88 \pm 0.70}$. This is to be compared with the derived BCES bisector $M_{\text{BH}} - C_{\text{FUV,tot}}$ and $M_{\text{BH}} - C_{\text{NUV,tot}}$ relations for the late-type galaxies having shallower slopes of 1.03 ± 0.13 and 1.38 ± 0.23 , such that $M_{\text{BH}} \propto (L_{\text{FUV,tot}}/L_{3.6,\text{tot}})^{-2.58 \pm 0.33}$ and $M_{\text{BH}} \propto (L_{\text{NUV,tot}}/L_{3.6,\text{tot}})^{-3.45 \pm 0.58}$.

With the assumption that the UV-to-3.6 μm luminosity ratio ($L_{\text{UV}}/L_{3.6}$) is a proxy for specific star formation rate, sSFR, (e.g., Bouquin et al. 2018), it implies that the growth of black holes in late-type galaxies have a steeper dependence on sSFR (i.e., $M_{\text{BH}} \propto \text{sSFR}_{\text{FUV}}^{-2.58}$) than early-type galaxies ($M_{\text{BH}} \propto \text{sSFR}_{\text{FUV}}^{-4.38}$). That is, at a given value of sSFR, late-type galaxies tend to have more massive BHs than early-type galaxies. The caveat of using FUV magnitudes as a proxy for the current star formation rate is that a significant fraction of the FUV light in $\sim 5\%$ of massive early-type galaxies may come from extreme horizontal branch stars instead of young upper main sequence stars, a phenomenon dubbed ‘UV upturn’ (e.g., Code & Welch 1979; O’Connell 1999; Yi et al. 2011). This is likely due to the rarity of very massive early-type galaxies in our sample. Nonetheless, we found that none of our early-type galaxies are UV upturns, when using the criteria given by Yi et al. (2011, their Table 1). Owing to a stronger sensitivity of the

FUV-band to the galaxy star formation rate (SFR) than the NUV-band, the $M_{\text{BH}} - C_{\text{FUV,tot}}$ relations are systematically shallower than the corresponding $M_{\text{BH}} - C_{\text{NUV,tot}}$ relations, although they are consistent with overlapping 1σ uncertainties (Table 1).

The root-mean-square (rms) scatter (Δ) around the fitted BCES bisector relations in the $\log M_{\text{BH}}$ direction are $\Delta_{\text{FUV,early}} \sim 0.86$ dex, $\Delta_{\text{FUV,late}} \sim 0.87$ dex, $\Delta_{\text{NUV,early}} \sim 0.72$ dex and $\Delta_{\text{NUV,late}} \sim 0.86$ dex. We report intrinsic scatters (ϵ) for our $M_{\text{BH}} - C_{\text{UV,tot}}$ relations as derived by LINMIX_ERR to be $\epsilon_{\text{FUV,early}} \sim 0.69 \pm 0.20$, $\epsilon_{\text{FUV,late}} \sim 0.69 \pm 0.22$, $\epsilon_{\text{NUV,early}} \sim 0.66 \pm 0.18$ and $\epsilon_{\text{NUV,late}} \sim 0.66 \pm 0.18$.

As noted previously, the LINMIX_ERR code and MCMC Bayesian analysis—which do account for the 24 galaxies (22 late-type galaxies and 2 early-type galaxies) with M_{BH} upper limits—yield $M_{\text{BH}} - C_{\text{UV,tot}}$ relations consistent with the BCES regression analyses (Table 1). Nonetheless, we checked for a potential bias for the late-type galaxies due to the inclusion of M_{BH} upper limits by rerunning the BCES bisector regression analysis on the 23 (=45-22) late-type galaxies with more securely measured M_{BH} . We find that the slopes, intercepts and Δ of the $M_{\text{BH}} - C_{\text{UV,tot}}$ relations are only weakly influenced by the exclusion of M_{BH} upper limits³. Including the upper limits in the black hole scaling relations is useful (Gültekin et al. 2009), given they also follow the $M - \sigma$ relation traced by galaxies with more securely measured M_{BH} (Fig. 3).

We can compare our work to that of Terrazas et al.

³ The strength of the $M_{\text{BH}} - C_{\text{UV,tot}}$ correlations decreases when the SMBH upper limits are excluded. The Pearson correlation coefficient for the $(C_{\text{FUV,tot}}, M_{\text{BH}})$ blue sequence has reduced from $r \sim 0.60$ to 0.34 due to the exclusion of M_{BH} upper limits, and for the $(C_{\text{NUV,tot}}, M_{\text{BH}})$ blue sequence there is a decrease in r from ~ 0.65 to 0.36.

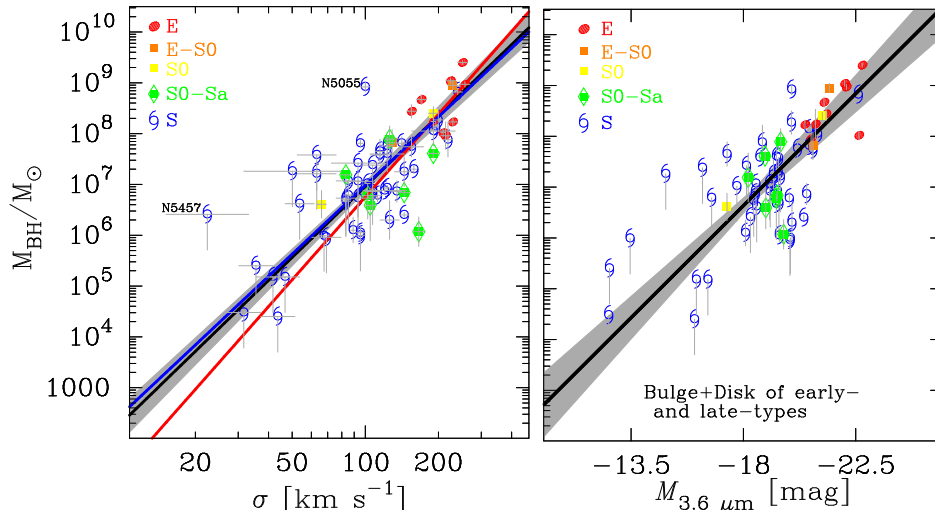


FIG. 3.— Similar to Fig. 2, but shown here are correlations between M_{BH} and (left panel) velocity dispersion (σ , van den Bosch 2016, his Table 2) and (right panel) total $3.6 \mu\text{m}$ absolute magnitude of our sample galaxies ($M_{3.6 \mu\text{m}}$). $M_{3.6 \mu\text{m}}$ are computed using the total $3.6 \mu\text{m}$ apparent magnitudes ($m_{3.6 \mu\text{m}}$, Table 5) and distances for the galaxies from van den Bosch (2016, his Table 2). We did not fit separate linear regressions to our early- and late-type (M_{BH} , $M_{3.6 \mu\text{m}}$) data or to the core-Sérsic and Sérsic (M_{BH} , $M_{3.6 \mu\text{m}}$) data, see the text for more details.

(2017, their Figs. 1 and 2) who used star formation rates (SFRs) determined based on *IRAS* far-infrared imaging and reported an inverse correlation between specific star formation rate (sSFR) and SMBH mass for 91 galaxies with measured black hole masses. Although they did not separate the galaxies into late- and early-types, their full sample seems to follow a single $M_{\text{BH}} - \text{sSFR}$ relation with no break, contrary to our results. To explain this discrepancy, we split the galaxies in Terrazas et al. (2017) by morphology and find that their late-type galaxies (which constitute a third of the full sample) reside at the low mass end of their $M_{\text{BH}} - \text{sSFR}$ relation and they span very small ranges in SMBH mass ($4 \times 10^6 \lesssim M_{\text{BH}}/M_{\odot} \lesssim 10^8$) and in sSFR ($10^{-11} \lesssim \text{sSFR}/\text{yr}^{-1} \lesssim 8 \times 10^{-9}$), inadequate to establish the blue $M_{\text{BH}} - C_{\text{UV,tot}}$ sequence (Fig. 2). Furthermore, we note that the FIR flux may underestimate the actual SFR for low-mass late-type galaxies as most of these galaxies' UV photons are unobscured by dust and thus not reprocessed to FIR wavelengths (Catalán-Torrecilla et al. 2015). We also find that the Terrazas et al. (2017) early-type $M_{\text{BH}} - \text{sSFR}$ relation has more scatter than that of ours. We suspect this may be due to a variable contamination of the *IRAS* FIR emissions in massive galaxies by the AGN⁴ which heats the surrounding dust. While the dusty AGN in some massive galaxies might lead to an increase in the SFR values based on FIR luminosities (e.g., Catalán-Torrecilla et al. 2015; Toba et al. 2017), star formation activities are likely the dominant contributor to the SFR values reported by Terrazas et al. (2017), AGN contamination being mainly responsible for the larger scatter observed their $M_{\text{BH}} - \text{sSFR}$ relation.

3.5. $M_{\text{BH}} - \sigma$ and $M_{\text{BH}} - L$ relations

In Fig. 2 we have shown, for the first time to our knowledge, a correlation between SMBH mass and total (i.e.,

⁴ While the IR emissions in massive galaxies have contributions from the dusty AGN, the NUV emissions arise from main-sequence turn-off stars and are less prone to contamination from the AGN (Boselli et al. 2005).

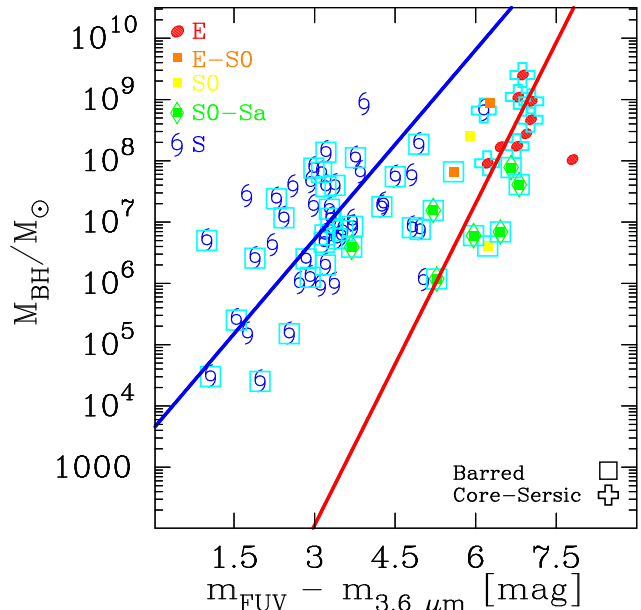


FIG. 4.— Similar to Fig. 2(a), but here we also show host galaxy properties. Barred galaxies are enclosed in boxes. Seven core-Sérsic galaxies (6 Es + 1 S) with partially depleted cores published in the literature are enclosed in crosses (see Section 4.2).

bulge+disk) colors for early- and late-type galaxies. For such a correlation to be evident, it is important that the color is determined using a wide wavelength baseline. In this section, we present correlations between M_{BH} and velocity dispersion (σ) and $3.6 \mu\text{m}$ total luminosity ($L_{3.6,\text{tot}}$) for the same galaxy sample to allow a direct statistical comparison with the $M_{\text{BH}} - C$ relations (Fig. 3 and Table 2). Assuming a 10% uncertainty⁵ on σ , the BCES bisector regression yields $M_{\text{BH}} - \sigma$ relations with slopes 5.42 ± 0.90 , 4.49 ± 0.48 and 4.65 ± 0.35 for the early-type galaxies, late-type galaxies and

⁵ After comparing the HyperLeda individual velocity dispersion measurements and mean homogenized values for 100 sample galaxies, we adopt a conservative upper limit uncertainty of 10% on σ .

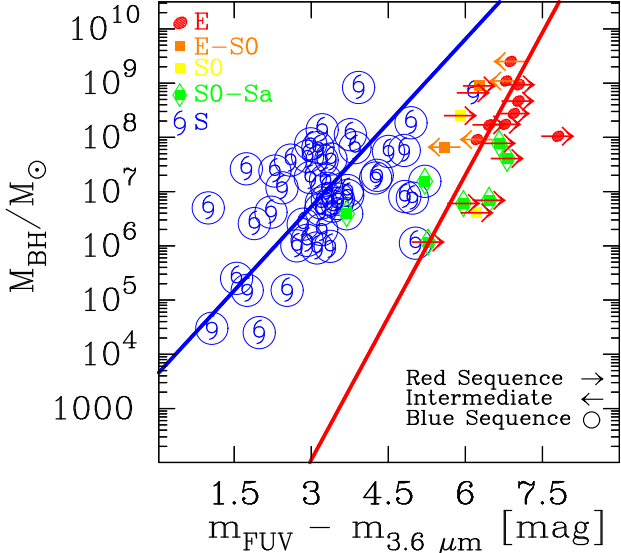


FIG. 5.— Similar to Fig. 2, but here comparing the $M_{\text{BH}} - C$ red and blue sequences and the color-color red/intermediate and blue sequences. The color-color relation red and intermediate sequence galaxies (Bouquin et al. 2018, their section 4.4) are marked by rightward- and leftward-pointing arrows, respectively, blue sequence galaxies are enclosed in circles.

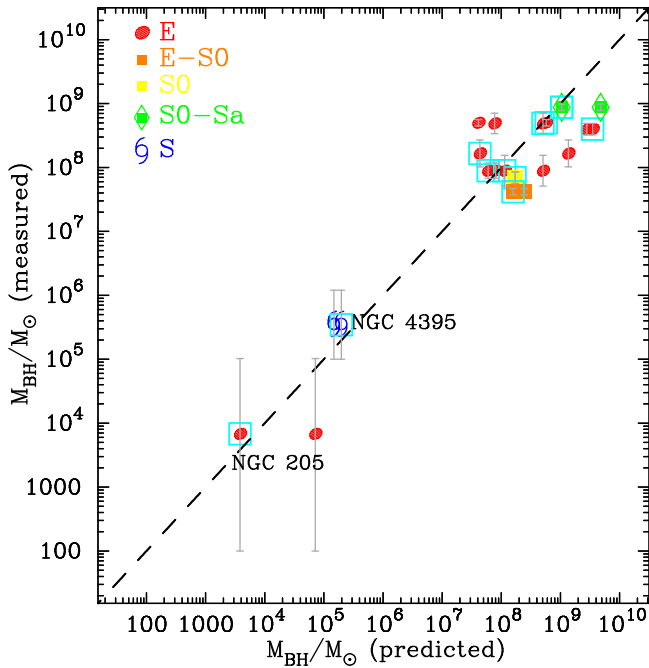


FIG. 6.— Comparison between SMBH masses predicted using our $M_{\text{BH}} - C_{\text{FUV,tot}}$ and $M_{\text{BH}} - C_{\text{NUV,tot}}$ relations (Table 1) and those determined dynamically (van den Bosch 2016; Nguyen et al. 2019) for a selected sample of 11 galaxies that are not in our sample (see Table 5). SMBH masses predicted based on the $M_{\text{BH}} - C_{\text{NUV,tot}}$ relations are enclosed in boxes.

for the full ensemble. These relations are in good agreement with each other within their 1σ uncertainties. The late-type galaxies NGC 5055 and NGC 5457, being the most deviant outliers in the $M_{\text{BH}} - \sigma$ diagram, were excluded. The unification of early- and late-type galaxies in the $M_{\text{BH}} - \sigma$ diagram is nothing new (e.g., Beifiori et al. 2012; Graham & Scott 2013; van den Bosch 2016; Dullo et al. 2020, submitted). The $M_{\text{BH}} - \sigma$ relations (Ta-

ble 2) are consistent with those from Gültekin et al. (2009), Beifiori et al. (2012); McConnell & Ma (2013); Kormendy & Ho (2013); Graham & Scott (2013)⁶.

To determine the $M_{\text{BH}} - L_{3.6,\text{tot}}$ relation, we converted the inclination and dust corrected $3.6 \mu\text{m}$ total apparent magnitudes into absolute magnitudes ($M_{3.6,\text{tot}}$, Appendix C) using distances given in van den Bosch (2016). The BCES bisector $M_{\text{BH}} - L_{3.6,\text{tot}}$ relation for the full sample of 67 galaxies was performed without accounting for the error on $M_{3.6,\text{tot}}$, yielding $M_{\text{BH}} \propto L_{3.6,\text{tot}}^{1.23 \pm 0.15}$ (Fig. 3 and Table 3). Graham & Scott (2013) reported two distinct $M_{\text{BH}} - L$ relations for the bulges of Sérsic galaxies ($M_{\text{BH}} \propto L_{\text{Ks,bulge}}^{2.73}$) and core-Sérsic galaxies ($M_{\text{BH}} \propto L_{\text{Ks,bulge}}^{1.10}$). Since there are only 7 galaxies we were able to identify as core-Sérsic galaxies (see Fig. 4), we refrain from separating the galaxies into Sérsic and core-Sérsic galaxies in the $M_{\text{BH}} - L_{3.6,\text{tot}}$ diagram.

4. DISCUSSION

4.1. Comparison between the $M_{\text{BH}} - C$, $M_{\text{BH}} - \sigma$ and $M_{\text{BH}} - L$ relations

Due to the different number of galaxies used to define the $M_{\text{BH}} - C$, $M_{\text{BH}} - \sigma$ and $M_{\text{BH}} - L$ relations, a direct comparison of the strength and scatter of the relations is difficult. Nonetheless, the correlation between the color $C_{\text{UV,tot}}$ and BH mass M_{BH} ($r \sim 0.60 - 0.70$, see Table 1) is slightly weaker than that between the stellar velocity dispersion σ and M_{BH} ($r \sim 0.72 - 0.78$, Table 2). These two relations have comparable intrinsic scatter (See Tables 1 and 2). In terms of scatter in the log M_{BH} direction, the $M_{\text{BH}} - C_{\text{UV,tot}}$ relations have typically 5%–27% more scatter (i.e., $\Delta \sim 0.72 - 0.87$ dex) than the $M_{\text{BH}} - \sigma$ relations ($\Delta \sim 0.68 - 0.70$ dex). The $M_{\text{BH}} - \sigma$ relation appears to be the most fundamental SMBH scaling relation. However, the $M_{\text{BH}} - \sigma$ relations for late- and early-type galaxies are not notably offset from each other. This contrasts with the formation models of galaxies which predict the SMBH growth in the two Hubble types to be completely different (see Section 4.5). Furthermore, in Dullo et al. (2020, submitted) we showed that the $M_{\text{BH}} - \sigma$ relation tends to underpredict the actual BH masses for the most massive galaxies with $M_* \gtrsim 10^{12} M_{\odot}$. In contrast, the $M_{\text{BH}} - C_{\text{UV,tot}}$ relations are in accordance with models of galaxy formation (Section 4.5).

As for the comparison between the $M_{\text{BH}} - C$ and $M_{\text{BH}} - L$ relations, these two relations display similar level of strength and vertical scatter (Table 3, $r \sim 0.60 - 0.70$ and $\Delta \sim 0.72 - 0.87$ dex for $M_{\text{BH}} - C_{\text{UV,tot}}$ and $r \sim -0.66$, and $\Delta \sim 0.84$ dex for $M_{\text{BH}} - L_{3.6,\text{tot}}$). In passing, we note that the existence of the $M_{\text{BH}} - L$ relation coupled with the red sequence and blue cloud traced by early- and late-type galaxies in the color-magnitude diagram does not necessitate a correlation between the black hole mass and galaxy color.

For comparison, our $M_{\text{BH}} - C_{\text{UV,tot}}$ relation for the 47 late-type galaxies is stronger ($r \sim 0.60 - 0.65$, and

⁶ Our slopes for the full sample of 66 galaxies are slightly (i.e., $\sim 1.4\sigma \approx 15\%$) shallower than that of van den Bosch (2016, slope $\sim 5.35 \pm 0.23$). This is because the van den Bosch (2016, his Fig. 1) sample contains extremely bright galaxies with $\sigma \gtrsim 270$ which tend to steepen the $M_{\text{BH}} - \sigma$ relation (see Fig. 1).

$\Delta \sim 0.87$ dex) than the $M_{\text{BH}} - M_{*,\text{tot}}$ relation based on $3.6 \mu\text{m}$ data by [Davis et al. \(2018\)](#) for their sample of 40 late-type galaxies ($r \sim 0.47$ and $\Delta \sim 0.79$ dex).

4.2. Core-Sérsic versus Sérsic

As noted in the Introduction, SMBH scaling relations may differ depending on the galaxy core structure (i.e., Core-Sérsic versus Sérsic type). We identify seven core-Sérsic galaxies (6 Es + 1 S) in our sample with partially depleted cores published in the literature: NGC 1052 ([Lauer et al. 2007](#)), NGC 3608, NGC 4278 and NGC 4472 ([Dullo & Graham 2012, 2014](#)), and NGC 4374, NGC 4594 and NGC 5846 ([Graham & Scott 2013](#)). They are among the reddest ($\mathcal{C}_{\text{FUV,tot}} \gtrsim 6$) galaxies in our sample with massive SMBHs ($M_{\text{BH}} \gtrsim 10^8 M_{\odot}$), Fig. 4. While structural analysis of high-resolution *HST* images are needed to identify a partially depleted core (or lack thereof) in the remaining sample galaxies (e.g., [Dullo & Graham 2013, 2014](#); [Dullo et al. 2016, 2017, 2018](#), the majority ($\sim 80\%$) of our spiral galaxies have $\sigma \lesssim 140 \text{ km s}^{-1}$ and they are likely Sérsic galaxies with no partially depleted cores (e.g., [Dullo & Graham 2012, 2013, 2014](#); [Dullo et al. 2017](#)). For early-type galaxies, we did not find bends or offsets from the $M_{\text{BH}} - \mathcal{C}_{\text{UV,tot}}$ relations because of core-Sérsic or Sérsic galaxies (Fig. 4).

4.3. Red, intermediate and blue sequences

To locate our galaxies in color-color diagrams, we used the classification by [Bouquin et al. \(2018\)](#), their section 4.4) who compared the (FUV –NUV) and (NUV [3.6]) colors to separate their galaxies into red, intermediate and blue sequences. Fig. 5 shows excellent coincidence between the red and blue $M_{\text{BH}} - \mathcal{C}$ (early- and late-type) morphological sequences (Sections 3.4) and the canonical color-color relation (red/intermediate) and blue sequences, respectively, only with three exceptions (NGC 2685, NGC 4245 and NGC 4594). The case of NGC 2685 was discussed in Section B.1.4. NGC 4245 is a barred S0-Sa galaxy with a prominent ring ([Treuthardt et al. 2007](#)). The spiral Sa NGC 4594 (also referred to as the Sombrero Galaxy) exhibits properties similar to massive early-type galaxies. [Spitler et al. \(2008\)](#) found that the number of blue globular cluster in NGC 4594 is comparable to massive early-type galaxies. Also, [Jardel et al. \(2011\)](#) noted that the galaxy’s dark matter density and core radius resemble those expected for early-type galaxies with massive bulges. It is the only red-sequence spiral in our sample ([Bouquin et al. 2018](#)), which is also unique in being the only core-Sérsic late-type galaxy in the sample. Interestingly, Fig. 5 reveals that all the intermediate sequence galaxies ([Bouquin et al. 2018](#)) reside toward the left of the $M_{\text{BH}} - \mathcal{C}_{\text{UV,tot}}$ relation defined by early-type galaxies.

4.4. Predicting SMBH masses using $M_{\text{BH}} - \mathcal{C}_{\text{UV}}$ relations

It is of interest to assess the robustness of BH masses estimated using the $M_{\text{BH}} - \mathcal{C}_{\text{FUV,tot}}$ and $M_{\text{BH}} - \mathcal{C}_{\text{NUV,tot}}$ relations found in this work. We do so using literature FUV, NUV and $3.6 \mu\text{m}$ magnitudes for a selected sample of 11 galaxies with direct SMBH masses that are not in our sample (see Table 4). These 11 galaxies were not included in the main sample as we

endeavor to establish the $M_{\text{BH}} - \mathcal{C}_{\text{UV,tot}}$ relations using homogeneously determined UV and $3.6 \mu\text{m}$ magnitudes. Doing this, the observed trends in the $M_{\text{BH}} - \mathcal{C}_{\text{UV,tot}}$ diagrams (Fig. 2) cannot be attributed to differences in methodologies and/or data sources. We use the BH mass measurement of NGC 205 by [Nguyen et al. \(2019\)](#) and for the remaining 10 galaxies the SMBH masses are from [van den Bosch \(2016\)](#). Of the 11 galaxies, 9 are in common between [Jeong et al. \(2009\)](#) and [Savorgnan & Graham \(2016\)](#). [Jeong et al. \(2009\)](#), their table 1) published total apparent FUV and NUV magnitudes derived from growth curves for the galaxies, while [Savorgnan & Graham \(2016\)](#), their table 2) presented their $3.6 \mu\text{m}$ galaxy apparent magnitudes⁷ which were computed using their best-fitting structural parameters. We also included the low-mass elliptical galaxy NGC 205 and the Seyfert SAM bulge-less galaxy NGC 4395 ([Filippenko & Ho 2003](#); [Peterson et al. 2005](#)). NGC 205 potentially harbors the lowest central BH mass measured for any galaxy to date ([Nguyen et al. 2019](#)) and NGC 4395 is known for being an outlier from the $M_{\text{BH}} - \sigma$ diagrams (e.g., [Davis et al. 2017](#)). For NGC 205, we use the UV and $3.6 \mu\text{m}$ magnitudes from [Gil de Paz et al. \(2007\)](#) and [Marleau et al. \(2006\)](#), respectively. For NGC 4395, the total UV and $3.6 \mu\text{m}$ magnitudes are from [Dale et al. \(2009\)](#) and [Lee et al. \(2011\)](#); a caveat here is that these magnitudes are not corrected for internal dust attenuation.

Before applying our $M_{\text{BH}} - \mathcal{C}_{\text{UV,tot}}$ relations to estimate M_{BH} , we homogenize the FUV, NUV and $3.6 \mu\text{m}$ data from the literature by comparing our magnitudes with those from [Jeong et al. \(2009\)](#) and [Savorgnan & Graham \(2016\)](#) for galaxies in common with them. We find that, compared to our magnitudes, the [Jeong et al. \(2009\)](#) total FUV and NUV magnitudes are fainter typically by 0.52 mag, while the galaxy magnitudes from [Savorgnan & Graham \(2016\)](#) are brighter typically by 0.18 mag. Having applied these corrections (i.e., $m_{\text{UV}} = m_{\text{UV,Jeon}} - 0.52$ and $m_{3.6} = m_{3.6,\text{Sav}} + 0.18$) for the 9 early-type galaxies, we computed the $\mathcal{C}_{\text{FUV,tot}}$ and $\mathcal{C}_{\text{NUV,tot}}$ colors listed in Table 4.

Fig. 6 reveals good agreement between the directly measured M_{BH} and predicted M_{BH} determined using $M_{\text{BH}} - \mathcal{C}_{\text{FUV,tot}}$ and $M_{\text{BH}} - \mathcal{C}_{\text{NUV,tot}}$ relations for the 10 galaxies in Table 4. On average, $|\log(M_{\text{BH,predicted}}/M_{\text{BH,measured}})| \sim 0.67 \text{ dex} \pm 0.29 \text{ dex}$ (FUV) and $\sim 0.32 \text{ dex} \pm 0.29 \text{ dex}$ (NUV). In Fig. 6, the direct BH mass appear to correlate better with that predicted using the NUV color than using the FUV color, and for the massive early-type galaxies, this may be due to contributions to the FUV flux from the extreme horizontal branch stars (see Section 3.4). The approach of using homogenized galaxy colors obtained through different methods may introduce some systematic errors in the determination M_{BH} . We caution that when using the $M_{\text{BH}} - \mathcal{C}$ relations to predict BH masses, one should use FUV, NUV and $3.6 \mu\text{m}$ magnitudes obtained in a homogeneous way. Furthermore, the $M_{\text{BH}} - \mathcal{C}$ relations *should not* be used to predict BH masses in galaxies that are highly inclined (e.g., edge-on) and obscured with dust.

As noted in the introduction, a clear benefit of the

⁷ We have converted the $3.6 \mu\text{m}$ VEGA magnitudes from [Savorgnan & Graham \(2016\)](#) into AB magnitudes.

TABLE 4
SUPERMASSIVE BLACK HOLE MASSES

Galaxy	Type	$C_{\text{UV,tot}}$ [AB mag] (FUV/NUV)	$\log(M_{\text{BH}}/M_{\odot})$ (directly measured)	$\log(M_{\text{BH}}/M_{\odot})$ (predicted) (FUV/NUV)
(1)	(2)	(3)	(4)	(5)
NGC 0205	E5 pec	4.61/2.67	$3.83^{+1.18}_{-1.83}$	4.85/3.58
NGC 0524	SA0	7.30/5.48	$8.94^{+0.05}_{-0.05}$	9.68/9.02
NGC 0821	E6	7.02/4.69	$8.22^{+0.21}_{-0.21}$	9.13/7.64
NGC 1023	SB0	6.64/5.01	$7.62^{+0.05}_{-0.05}$	8.39/8.20
NGC 4395	SAm	1.49/1.37	$5.54^{+0.54}_{-0.54}$	5.17/5.29
NGC 4459	SA0	6.56/5.03	$7.84^{+0.09}_{-0.09}$	8.24/8.23
NGC 4473	E5	6.80/4.93	$7.95^{+0.24}_{-0.24}$	8.71/8.06
NGC 4552	E	6.24/5.33	$8.70^{+0.05}_{-0.05}$	7.61/8.76
NGC 4564	E6	6.34/4.77	$7.95^{+0.12}_{-0.12}$	7.91/7.78
NGC 4621	E5	7.18/5.78	$8.60^{+0.09}_{-0.09}$	9.41/9.55
NGC 5845	E	6.38/5.30	$8.69^{+0.16}_{-0.16}$	7.89/8.71

Notes.— Col. (1) galaxy name. Col. (2) morphological type from NED. Col. (3) total FUV- [3.6] and NUV- [3.6] colors ($C_{\text{FUV,tot}}$ and $C_{\text{NUV,tot}}$). Cols. (4) directly measured SMBH masses. Cols. (5) BH masses predicted using the $M_{\text{BH}} - C_{\text{FUV,tot}}$ and $M_{\text{BH}} - C_{\text{NUV,tot}}$ relations (Table 1) and the appropriate colors given in Col. (3). We assign a typical uncertainty of 0.85 dex on $\log(M_{\text{BH}})$ for these predicted BH masses.

$M_{\text{BH}} - C_{\text{UV,tot}}$ relation is its applicability to early- and late-type galaxies including those with low central velocity dispersions ($\sigma \lesssim 100 \text{ km s}^{-1}$) and with small or no bulges. Moreover, photometry has the advantage of being cheaper than spectroscopy. Using our relations (Table 1) together with galaxy colors derived from the Bouquin et al. (2018, their Table 1) asymptotic FUV, NUV and $3.6 \mu\text{m}$ magnitudes, we tentatively predict BH masses in a sample of 1382 *GALEX*/*S*⁴*G* galaxies (Table 6) with no measured BH masses, see Appendix D. We show that late-type galaxies with $C_{\text{FUV,tot}} \lesssim 1.33$ AB mag or $C_{\text{NUV,tot}} \lesssim 1.28$ AB mag may harbor intermediate-mass black holes ($M_{\text{BH}} \sim 100 - 10^5 M_{\odot}$). Similarly, early-type galaxies with $C_{\text{FUV,tot}} \lesssim 4.68$ AB mag or $C_{\text{NUV,tot}} \lesssim 3.4$ AB mag are potential IMBH hosts. While Sloan Digital Sky Survey (SDSS) velocity dispersion measurements are available for hundreds of thousands of galaxies and one can use them together with the $M_{\text{BH}} - \sigma$ relation to estimate BH masses, as cautioned by SDSS Data Release⁸ 12 (Alam et al. 2015), velocity dispersion values less than 100 km s^{-1} reported by SDSS are below the resolution limit of the SDSS spectrograph and are regarded as unreliable. Note that galaxies with $\sigma \lesssim 100 \text{ km s}^{-1}$ are expected to have low stellar masses ($M_{\star} \lesssim 2 \times 10^{10} M_{\odot}$), and such galaxies make up a significant fraction of the SDSS galaxy sample (Chang et al. 2015, see their Fig. 9). In addition, the SDSS spectra measure the light within a fixed aperture of radius $1''.5$, thus the SDSS velocity dispersion values of more distant galaxies can be systematically lower than those of similar, nearby galaxies.

⁸ <https://www.sdss.org/dr12/algorithms/redshifts/>

4.5. The $M_{\text{BH}} - C_{\text{UV}}$ correlation as evidence for the co-evolution of SMBHs and galaxies

Morphologically splitting the sample galaxies, we have demonstrated that late-type hosts do not correlate with SMBHs in the same manner as early-type hosts (Table 1). This reconciles very well with the prediction that early- and late-type galaxies have fundamentally different formation histories (e.g., White & Rees 1978; Khochfar & Burkert 2001; Steinmetz & Navarro 2002; Kauffmann et al. 2003a; Kormendy & Kennicutt 2004; Schawinski et al. 2010; Dullo & Graham 2014; Schawinski et al. 2014; Tonini et al. 2016; Davis et al. 2018; Dullo et al. 2019). For example, the red and blue $M_{\text{BH}} - C_{\text{FUV,tot}}$ relations are such that $M_{\text{BH,early-type}} \propto (L_{\text{FUV,tot}}/L_{3.6,\text{tot}})^{-4.38}$ and $M_{\text{BH,late-type}} \propto (L_{\text{FUV,tot}}/L_{3.6,\text{tot}})^{-2.58}$. Given that $L_{\text{UV}}/L_{3.6}$ is a good proxy for the sSFR, (Bouquin et al. 2018, their Appendix B), it therefore implies that both early- and late-type galaxies exhibit log-linear inverse correlations between M_{BH} and sSFR, the latter having a steeper dependence on sSFR than the former (see Table 1 and Fig. 2).

A correlation between M_{BH} and sSFR is not unexpected. Observations have shown that bright quasars and local Seyferts tend to reside in strong starburst galaxies or in galaxies with an ongoing star formation (e.g., Sanders et al. 1988; Kauffmann et al. 2003b; Alexander et al. 2005; Lutz et al. 2008; Netzer 2009; Wild et al. 2010; Rosario et al. 2012; Yang et al. 2017; Barrows et al. 2017). Other findings lending further support to the link between star formation and SMBH growth are the correlation between black hole accretion rate and host galaxy star formation rate (e.g., Merloni et al. 2004; Heckman et al. 2004; Hopkins & Quataert 2010; Chen et al. 2013; Madau & Dickinson 2014; Sijacki et al. 2015; Yang et al. 2017), the inverse correlation between sSFR and specific supermassive black hole mass (Terrasas et al. 2017) and the trend between SMBH mass and host galaxy star formation histories over cosmic time (e.g., Martín-Navarro et al. 2018; van Son et al. 2019).

Within the self-regulated SMBH growth model, the correlation between SMBH masses and the host galaxy properties (e.g., stellar luminosity, McLure & Dunlop 2002; Marconi & Hunt 2003) is interpreted as reflecting a link between the growth of SMBHs and star formation events in the host (Silk & Rees 1998; Fabian 1999; King 2003; Springel et al. 2005; Di Matteo et al. 2005; Murray et al. 2005; Croton et al. 2006; Hopkins et al. 2006; Schawinski et al. 2006; Cattaneo et al. 2009; Weinberger et al. 2017). In this scenario, the same cold gas reservoir that fuels the AGN/quasar, feeds starburst events. The energy or momentum released by the AGN/quasar can heat the interstellar medium and cause the expulsion of gas from the host galaxy, shutting off star formation and halting accretion onto the SMBH. However, whether AGN accretion and star formation are precisely coincidental is unclear (e.g., Ho 2005).

We (see also Dullo et al. 2020, submitted) argue that the significantly different $M_{\text{BH}} - C_{\text{FUV}}$ relations for early- and late-type galaxies (i.e., the $M_{\text{BH}} - C_{\text{FUV}}$ red and blue sequences) suggest that the two Hubble types follow two distinct channels of SMBH growth, the former

is major merger driven while the latter involves (major merger)-free processes (see [Hopkins & Hernquist 2009](#)), in broad accordance with [Schawinski et al. \(2010, 2014\)](#).

The standard cosmological formation paradigm is that SMBHs in early-type galaxies are built up during the period of rapid galaxy growth at high redshift ($z \sim 2-5$) when the major, gas-rich mergers of disk galaxies (e.g., [Toomre & Toomre 1972](#); [White & Rees 1978](#)) drives gas infall into the nuclear regions of the newly formed merger remnant, leading to starburst events and AGN accretion processes (e.g., [Barnes & Hernquist 1991, 1996](#); [Naab et al. 2006a](#); [Hopkins & Quataert 2010](#); [Knapen et al. 2015](#)). Accretion onto more massive SMBHs trigger stronger AGN feedback, efficient at quenching of star formation rapidly. As such, the position of an early-type galaxy on the $M_{\text{BH}} - C_{\text{UV}}$ red sequence is dictated by the complex interplay between the details of its SMBH growth, efficiency of AGN feedback, regulated star formation histories and major merger histories, rather than this being set by simple hierarchical merging ([Peng 2007](#); [Jahnke & Macciò 2011](#)).

Massive early-type galaxies (i.e., total stellar mass $M_{*,k} \sim 8 \times 10^{10} M_{\odot} - 10^{12} M_{\odot}$) with $M_{\text{BH}} \gtrsim 10^8 M_{\odot}$ and $C_{\text{FUV}} \gtrsim 6.3$ mag, at the high-mass end of the $M_{\text{BH}} - C_{\text{UV}}$ red sequence (Fig. 2, Section 4.3), are consistent with the scenario where (gas-rich) major merger at high redshift drives intense bursts of star formation, efficient SMBH growth and ensuing quenching of star formation by strong AGN feedback in short timescales (e.g., [Thomas et al. 2005, 2010](#); [de La Rosa et al. 2011](#); [McDermid et al. 2015](#); [Segers et al. 2016](#)). This is accompanied by a few (0.5–2) successive gas-poor (dry) major mergers since $z \sim 1.5 - 2$ (e.g., [Bell et al. 2004, 2006](#); [Khochfar & Silk 2009](#); [Man et al. 2012](#); [Dullo & Graham 2012, 2013, 2014](#); [Rodríguez-Gomez et al. 2015](#)), involving low level star formation⁹ (i.e., ‘red but not strictly dead’, see [de La Rosa et al. 2011](#); [Habouzit et al. 2019](#); [Davis et al. 2019](#)) detected by the *GALEX* FUV and NUV detectors (e.g., [Gil de Paz et al. 2007](#); [Bouquin et al. 2018](#)). The bulk of these objects are core-Sérsic elliptical galaxies a fraction of which may gradually grow stellar disk structures and transform into massive lenticular galaxies ([Graham 2013](#); [Dullo & Graham 2013](#); [Dullo 2014](#); [Graham et al. 2015](#); [de la Rosa et al. 2016](#)).

As for the less massive (Sérsic) early-type galaxies ($M_{*,k} \sim 10^{10} M_{\odot} - 2 \times 10^{11} M_{\odot}$) with smaller SMBH masses ($10^6 M_{\odot} \lesssim M_{\text{BH}} \lesssim 10^8 M_{\odot}$) and $C_{\text{FUV}} \lesssim 6.3$ mag (Fig. 2, Section 4.3) likely grow primarily via gas-rich (wet) major mergers and form their stellar populations over an extended period of time ([Thomas et al. 2005, 2010](#); [de La Rosa et al. 2011](#); [McDermid et al. 2015](#)). Our findings disfavor a scenario where Sérsic early-type galaxies with intermediate colors are late-type galaxies quenching star formation and moving away from the $M_{\text{BH}} - C_{\text{FUV}}$ blue sequence. Collectively, core-Sérsic and

Sérsic early-type galaxies define a red sequence in the $M_{\text{BH}} - C_{\text{FUV}}$ diagram. Lacking the most luminous and massive BCGs with $M_{*,k} \gtrsim 10^{12} M_{\odot}$ in our sample, we note that our $M_{\text{BH}} - C_{\text{UV}}$ relation is not constrained at the highest-mass end. Since such galaxies are generally expected to have negligible star formation ([Dullo 2019](#)), the $M_{\text{BH}} - C_{\text{UV}}$ relations, the $M_{\text{BH}} - C_{\text{FUV}}$ in particular, may not apply to them. Our interpretation of the assembly of the red sequence for early-type galaxies is in accordance with the ‘downsizing’ scenario, where more massive galaxies form stars earlier and over a shorter time scale than less massive galaxies (e.g., [Cowie et al. 1996](#); [Brinchmann & Ellis 2000](#); [Cattaneo et al. 2008](#); [Pérez-González et al. 2008](#); [Pannella et al. 2009](#)).

The (major merger)-free scenario—secular processes and minor mergers—may be naturally consistent with the observed late-type $M_{\text{BH}} - C_{\text{FUV}}$ blue sequence (Fig. 2, Section 4.3) and dynamically cold stellar disks of late-type galaxies. Recently, [Martin et al. \(2018a\)](#) reported that massive SMBHs in disk galaxies can grow primarily via secular processes with small contributions (i.e., only 35 % of the SMBH mass) from mergers. We tentatively hypothesize secular-driven processes involving non-axisymmetric stellar structures, such as bars and spiral arms can trigger a large inflow of gas from the large scale disk into nuclear regions of late-type galaxies, slowly feeding SMBHs and fueling star formation (e.g., [Kormendy 1993](#); [Kormendy & Kennicutt 2004](#); [Fisher & Drory 2008](#); [Leitner 2012](#); [Kormendy 2013](#); [Cisternas et al. 2013](#); [Tonini et al. 2016](#); [Dullo et al. 2019](#)). Barred galaxies make up the bulk ($\sim 62\%$) of the late-type galaxies in our sample (Fig. 4). In addition, gas-rich minor mergers have been suggested in the literature to trigger enhanced star formation and SMBH growth in late-type galaxies without destroying the disks ([Simmons et al. 2013](#); [Kaviraj 2014b,a](#); [Simmons et al. 2017](#); [Martin et al. 2018b,a](#)). A question remains however whether pure (major merger)-free processes could be the main mechanism for the formation of late-type galaxies with massive bulges and high-velocity dispersion, as in the case of NGC 4594.

As noted above, we find that core-Sérsic¹⁰ and Sérsic galaxies collectively define a single early- or late-type morphology sequence, in agreement with the conclusions by [Sahu et al. \(2019\)](#); [Dullo \(2019\)](#); [Dullo et al. \(2020, submitted\)](#). Moreover, although [Savorgnan et al. \(2016\)](#) reported a blue, spiral galaxy $M_{\text{BH}} - M_{*,\text{bulge}}$ sequence, their sample of 17 spiral galaxies trace the red end of the blue $M_{\text{BH}} - M_{*,\text{bulge}}$ sequence ([Davis et al. 2018](#), their Section 2.2).

We remark that bulgeless spirals and spiral galaxies with classical bulges or pseudo-bulges all follow the blue, late-type $M_{\text{BH}} - C_{\text{UV}}$ relations (Fig. 2). Pseudo-bulges are hosted typically by late-type galaxies and a few early-type galaxies, while classical bulges are generally associated with early-type galaxies and massive late-type galaxies. A key point to note here is that the relatively high sSFR for pseudo-bulges coupled with the steeper dependence of SMBH masses on sSFRs for late-type galaxies likely explain why pseudo-bulges seem to obey a different $M_{\text{BH}} - \sigma$ relation than classical bulges

⁹ Massive early-type galaxies and some BCGs can acquire cold gas through the cooling of hot gas and/or via cannibalism of a gas-rich satellite and they may undergo episodes of low level star formation at low redshift ([Salomé & Combes 2003](#); [O’Dea et al. 2008](#); [Hopkins & Hernquist 2009](#); [Struve et al. 2010](#); [Young et al. 2011](#); [Zubovas & King 2012](#); [Russell et al. 2014](#); [Smith & Edge 2017](#); [Russell et al. 2019](#); [Krajinović et al. 2020](#)).

¹⁰ All the seven core-Sérsic galaxies in this paper are “normal-core” galaxies ([Dullo 2019](#)).

(e.g., Kormendy & Ho 2013). This also explains as to why bulgeless spirals and low-mass spirals offset from the $M_{\text{BH}} - L_{\text{Bulge}}$, $M_{\text{BH}} - M_{*,\text{Bulge}}$ and $M_{\text{BH}} - \sigma$ relations defined by the massive early- and late-type galaxies as reported in the literature (e.g., Greene et al. 2008, 2010, 2016; Baldassare et al. 2017).

5. CONCLUSIONS

Using a sample of 67 *GALEX*/*S*⁴*G* galaxies with directly measured supermassive black hole masses (M_{BH}), comprised of 20 early-type galaxies and 47 late-type galaxies, for the first time we establish a correlation between (M_{BH}) and the host galaxy total (i.e., bulge+disk) UV– [3.6] color (\mathcal{C}_{UV}). More massive SMBHs are hosted by galaxies with redder colors. The *GALEX* FUV/NUV and *S*⁴*G* *Spitzer* 3.6 μm asymptotic magnitudes of the sample galaxies determined in a homogeneous manner (Bouquin et al. 2018) along with their 3.6 μm multi-component decomposition by Salo et al. (2015) were used to derive dust-corrected total (bulge+disk) magnitudes in FUV, NUV and 3.6 μm bands. We provide these magnitudes in Table 5.

We fit our ($M_{\text{BH}}, \mathcal{C}_{\text{UV,tot}}$) dataset using several statistical techniques, focusing on the symmetric BCES bisector regressions. Our key findings are as follows.

(1) Investigating the nature of the $M_{\text{BH}} - \mathcal{C}_{\text{UV,tot}}$ relations, our results show that early-type galaxies define a red-sequence in the $M_{\text{BH}} - \mathcal{C}_{\text{UV,tot}}$ diagrams different from the late-type blue-sequence. We found a strong tendency for the galaxies which lie on the red/blue $M_{\text{BH}} - \mathcal{C}$ morphological sequences to also be on the (red plus intermediate)/blue sequences in the canonical color-color relation (See Section 4.3 and Fig. 5).

(2) The $M_{\text{BH}} - \mathcal{C}_{\text{FUV,tot}}$ and $M_{\text{BH}} - \mathcal{C}_{\text{NUV,tot}}$ relations for early-type galaxies have slopes of 1.75 ± 0.41 and 1.95 ± 0.28 , respectively, whereas for late-type galaxies the slopes are substantially shallower, i.e., 1.03 ± 0.13 and 1.38 ± 0.23 . The early- and late-type $M_{\text{BH}} - \mathcal{C}_{\text{UV,tot}}$ relations have root-mean-square (rms) scatters (Δ) in the $\log M_{\text{BH}}$ direction of $\Delta_{\text{UV,early}} \sim 0.72 - 0.86$ dex and $\Delta_{\text{UV,late}} \sim 0.86$ dex and Pearson correlation coefficients (r) of $r_{\text{early}} \sim 0.61 - 0.70$ and $r_{\text{late}} \sim 0.60 - 0.65$.

(3) Given $L_{\text{UV,tot}}/L_{3.6,\text{tot}}$ is a good proxy for specific star formation rate (sSFR), it follows that both early- and late-type galaxies exhibit log-linear inverse correlations between M_{BH} and sSFR, the latter having a steeper dependence on sSFR (i.e., $M_{\text{BH}} \propto \text{sSFR}_{\text{FUV}}^{-2.58}$) than the former ($M_{\text{BH}} \propto \text{sSFR}_{\text{FUV}}^{-4.38}$). This suggests different channels for SMBH growth in early- and late-type galaxies.

(4) We have compared the $M_{\text{BH}} - \mathcal{C}_{\text{UV,tot}}$ relations with the $M_{\text{BH}} - \sigma$ and $M_{\text{BH}} - L_{3.6,\text{tot}}$ relations for our sample galaxies. While the $M_{\text{BH}} - \mathcal{C}_{\text{UV}}$ relations are marginally weaker ($r \sim 0.60 - 0.70$) and have typically 5% – 27% more scatter than the $M_{\text{BH}} - \sigma$ relations ($r \sim 0.72 - 0.78$), the former potentially constrains SMBH-galaxy co-evolution models that predict different SMBH growth for different morphologies. In contrast, the $M - \sigma$ relations for late- and early-type galaxies are similar. The $M_{\text{BH}} - \mathcal{C}_{\text{UV,tot}}$ and $M_{\text{BH}} - L_{3.6,\text{tot}}$ relations display similar level of strength and vertical scatter.

(5) We did not detect departures (bends or offsets)

from the $M_{\text{BH}} - \mathcal{C}_{\text{UV,tot}}$ relations because of core-Sérsic or Sérsic galaxies. However, we cannot firmly rule out the presence of such substructures, as our sample does not consist of a large number of core-Sérsic galaxies.

(6) We argue that the different $M_{\text{BH}} - \mathcal{C}_{\text{UV}}$ relations for early- and late-type galaxies reflect that the two Hubble types have two distinct SMBH feeding mechanisms. *Massive early-type galaxies* ($M_{*,k} \sim 8 \times 10^{10} M_{\odot} - 10^{12} M_{\odot}$) at the high-mass end of the $M_{\text{BH}} - \mathcal{C}_{\text{UV}}$ red sequence, are core-Sérsic galaxies. Their formation is consistent with the scenario in which gas-rich (wet) major merger at high redshift drives intense bursts of star formation, efficient SMBH growth and the ensuing rapid quenching of star formation by strong AGN feedback. This is accompanied by gas-poor (dry) major mergers since $z \sim 1.5 - 2$, involving low level star formation. In contrast, the *less massive (Sérsic) early-type galaxies* ($M_{*,k} \sim 10^{10} M_{\odot} - 2 \times 10^{11} M_{\odot}$) at the low-mass part of the $M_{\text{BH}} - \mathcal{C}_{\text{UV}}$ red sequence are likely built-up primarily via gas-rich major mergers and form their stellar populations over an extended period of time. We tentatively hypothesize that *late-type galaxies* ($M_{*,k} \sim 10^9 M_{\odot} - 2 \times 10^{11} M_{\odot}$) which define the $M_{\text{BH}} - \mathcal{C}_{\text{UV}}$ blue sequence form via secular-driven processes involving non-axisymmetric stellar structures, such as bars and spiral arms. Gas-rich minor mergers could also account for the build-up of late-type galaxies.

(7) Having demonstrated the potential of our $M_{\text{BH}} - \mathcal{C}_{\text{UV}}$ relations to predict the SMBH masses in 10 galaxies, we employ these new relations to estimate the central BH masses in 1382 *GALEX*/*S*⁴*G* galaxies with no measured BH masses, after excluding highly inclined and dust obscured *GALEX*/*S*⁴*G* galaxies (Bouquin et al. 2018). We suggest the $M_{\text{BH}} - \mathcal{C}_{\text{UV}}$ relations can be used to estimate BH masses, without the need for high-resolution spectroscopy. However, we warn that to do so one should use galaxy colors determined based on UV and 3.6 μm magnitudes obtained in a homogeneous way. Furthermore, the $M_{\text{BH}} - \mathcal{C}_{\text{UV}}$ relations can be used to identify low-mass and bulgeless galaxies that potentially harbor intermediate-mass black holes.

6. ACKNOWLEDGMENTS

We thank the referee for their useful comments. B.T.D acknowledges support from a Spanish postdoctoral fellowship ‘Ayudas 1265 para la atracción del talento investigador. Modalidad 2: jóvenes investigadores.’ funded by Comunidad de Madrid under grant number 2016-T2/TIC-2039. B.T.D acknowledges support from grant ‘Ayudas para la realización de proyectos de I+D para jóvenes doctores 2019.’ funded by Comunidad de Madrid and Universidad Complutense de Madrid under grant number PR65/19-22417. We acknowledge financial support from the Spanish Ministry of Economy and Competitiveness (MINECO) under grant numbers AYA2016-75808-R and RTI, which is partly funded by the European Regional Development Fund, and from the Excellence Network MaegNet (AYA2017-90589-REDT). A.Y.K.B. acknowledges financial support from the Spanish Ministry of Economy and Competitiveness (MINECO), project Estallidos AYA2016-79724-C4-2-P. J.H.K. acknowledges financial support from the European Union’s Horizon 2020 research and innovation

programme under Marie Skłodowska-Curie grant agreement No 721463 to the SUNDIAL ITN network, from the State Research Agency (AEI) of the Spanish Ministry of Science, Innovation and Universities (MCIU) and the European Regional Development Fund (FEDER) under the grant with reference AYA2016-76219-P, from IAC project P/300724, financed by the Ministry of Science, Innovation and Universities, through the State Budget and

by the Canary Islands Department of Economy, Knowledge and Employment, through the Regional Budget of the Autonomous Community, and from the Fundación BBVA under its 2017 programme of assistance to scientific research groups, for the project “Using machine-learning techniques to drag galaxies from the noise in deep imaging”. J.G. acknowledges financial support from the Spanish Ministry of Economy and Competitiveness under grant number AYA2016-77237-C3-2P.

REFERENCES

- Akritas, M. G., & Bershad, M. A. 1996, *ApJ*, 470, 706
- Alam, S., Albareti, F. D., Allende Prieto, C., et al. 2015, *ApJS*, 219, 12
- Alexander, D. M., Smail, I., Bauer, F. E., et al. 2005, *Nature*, 434, 738
- Andreon, S., & Weaver, B. 2015, *Bayesian Methods for the Physical Sciences. Learning from Examples in Astronomy and Physics.*, doi:10.1007/978-3-319-15287-5
- Athanassoula, E. 2005, *MNRAS*, 358, 1477
- Bahcall, J. N., Kozlovsky, B.-Z., & Salpeter, E. E. 1972, *ApJ*, 171, 467
- Baldassare, V. F., Reines, A. E., Gallo, E., & Greene, J. E. 2017, *ApJ*, 850, 196
- Baldry, I. K., Glazebrook, K., Brinkmann, J., et al. 2004, *ApJ*, 600, 681
- Balick, B., & Heckman, T. 1981, *A&A*, 96, 271
- Barnes, J. E., & Hernquist, L. 1996, *ApJ*, 471, 115
- Barnes, J. E., & Hernquist, L. E. 1991, *ApJ*, 370, L65
- Barrows, R. S., Comerford, J. M., Zakamska, N. L., & Cooper, M. C. 2017, *ApJ*, 850, 27
- Begelman, M. C., Blandford, R. D., & Rees, M. J. 1980, *Nature*, 287, 307
- Beifiori, A., Courteau, S., Corsini, E. M., & Zhu, Y. 2012, *MNRAS*, 419, 2497
- Bell, E. F., Wolf, C., Meisenheimer, K., et al. 2004, *ApJ*, 608, 752
- Bell, E. F., Naab, T., McIntosh, D. H., et al. 2006, *ApJ*, 640, 241
- Bertola, F., Burstein, D., & Buson, L. M. 1993, *ApJ*, 403, 573
- Boselli, A., Cortese, L., Deharveng, J. M., et al. 2005, *ApJ*, 629, L29
- Bouquin, A. Y. K., Gil de Paz, A., Boissier, S., et al. 2015, *ApJ*, 800, L19
- Bouquin, A. Y. K., Gil de Paz, A., Muñoz-Mateos, J. C., et al. 2018, *ApJS*, 234, 18
- Brammer, G. B., Whitaker, K. E., van Dokkum, P. G., et al. 2009, *ApJ*, 706, L173
- Braun, R., Walterbos, R. A. M., Kennicutt, Jr., R. C., & Tacconi, L. J. 1994, *ApJ*, 420, 558
- Brinchmann, J., & Ellis, R. S. 2000, *ApJ*, 536, L77
- Buson, L. M., Bertola, F., Bressan, A., Burstein, D., & Cappellari, M. 2004, *A&A*, 423, 965
- Carollo, C. M., & Danziger, I. J. 1994, *MNRAS*, 270, 743
- Carollo, C. M., Stiavelli, M., de Zeeuw, P. T., & Mack, J. 1997, *AJ*, 114, 2366
- Carpenter, B., Gelman, A., Hoffman, M. D., et al. 2017, *Journal of Statistical Software*, Vol. 76, Issue 1, 2017, 76
- Catalán-Torrecilla, C., Gil de Paz, A., Castillo-Morales, A., et al. 2015, *A&A*, 584, A87
- Cattaneo, A., Dekel, A., Faber, S. M., & Guiderdoni, B. 2008, *MNRAS*, 389, 567
- Cattaneo, A., Faber, S. M., Binney, J., et al. 2009, *Nature*, 460, 213
- Chang, Y.-Y., van der Wel, A., da Cunha, E., & Rix, H.-W. 2015, *ApJS*, 219, 8
- Chen, C.-T. J., Hickox, R. C., Alberts, S., et al. 2013, *ApJ*, 773, 3
- Chester, C., & Roberts, M. S. 1964, *AJ*, 69, 635
- Cisternas, M., Gadotti, D. A., Knapen, J. H., et al. 2013, *ApJ*, 776, 50
- Code, A. D., & Welch, G. A. 1979, *ApJ*, 228, 95
- Conselice, C. J., Gallagher, J. S., Calzetti, D., Homeier, N., & Kinney, A. 2000, *AJ*, 119, 79
- Courteau, S., de Jong, R. S., & Broeils, A. H. 1996, *ApJ*, 457, L73
- Cowie, L. L., Songaila, A., Hu, E. M., & Cohen, J. G. 1996, *AJ*, 112, 839
- Croton, D. J., Springel, V., White, S. D. M., et al. 2006, *MNRAS*, 365, 11
- Dale, D. A., Cohen, S. A., Johnson, L. C., et al. 2009, *ApJ*, 703, 517
- Davis, B. L., Graham, A. W., & Cameron, E. 2018, *ApJ*, 869, 113
- Davis, B. L., Graham, A. W., & Seigar, M. S. 2017, *MNRAS*, 471, 2187
- Davis, T. A., Greene, J. E., Ma, C.-P., et al. 2019, *arXiv e-prints*, arXiv:1903.08884
- de La Rosa, I. G., La Barbera, F., Ferreras, I., & de Carvalho, R. R. 2011, *MNRAS*, 418, L74
- de la Rosa, I. G., La Barbera, F., Ferreras, I., et al. 2016, *MNRAS*, 457, 1916
- Di Matteo, T., Springel, V., & Hernquist, L. 2005, *Nature*, 433, 604
- Dressler, A. 1989, in *IAU Symposium, Vol. 134, Active Galactic Nuclei*, ed. D. E. Osterbrock & J. S. Miller, 217
- Driver, S. P., Popescu, C. C., Tuffs, R. J., et al. 2008, *ApJ*, 678, L101
- Dullo, B. T. 2014, *Astronomical Society of the Pacific Conference Series*, Vol. 480, *Central Stellar Mass Deficits in the Bulges of Local Lenticular Galaxies*, ed. M. S. Seigar & P. Treuthardt, 75
- . 2019, *ApJ*, 886, 80
- Dullo, B. T., & Graham, A. W. 2012, *ApJ*, 755, 163
- . 2013, *ApJ*, 768, 36
- . 2014, *MNRAS*, 444, 2700
- . 2015, *ApJ*, 798, 55
- Dullo, B. T., Graham, A. W., & Knapen, J. H. 2017, *MNRAS*, 471, 2321
- Dullo, B. T., Martínez-Lombilla, C., & Knapen, J. H. 2016, *MNRAS*, 462, 3800
- Dullo, B. T., Knapen, J. H., Williams, D. R. A., et al. 2018, *MNRAS*, 475, 4670
- Dullo, B. T., Chamorro-Cazorla, M., Gil de Paz, A., et al. 2019, *ApJ*, 871, 9
- Ebisuzaki, T., Makino, J., & Okumura, S. K. 1991, *Nature*, 354, 212
- Elmegreen, D. M., Chromey, F. R., McGrath, E. J., & Ostenson, J. M. 2002, *AJ*, 123, 1381
- Erwin, P., Saglia, R. P., Fabricius, M., et al. 2015, *MNRAS*, 446, 4039
- Eskridge, P. B., & Pogge, R. W. 1997, *ApJ*, 486, 259
- Faber, S. M., Tremaine, S., Ajhar, E. A., et al. 1997, *AJ*, 114, 1771
- Fabian, A. C. 1999, *MNRAS*, 308, L39
- Feigelson, E. D., & Babu, G. J. 1992, *ApJ*, 397, 55
- Ferrarese, L., & Ford, H. 2005, *Space Sci. Rev.*, 116, 523
- Ferrarese, L., & Merritt, D. 2000, *ApJ*, 539, L9
- Filippenko, A. V., & Ho, L. C. 2003, *ApJ*, 588, L13
- Fisher, D. B., & Drory, N. 2008, *AJ*, 136, 773
- Gadotti, D. A. 2009, *MNRAS*, 393, 1531
- García-Burillo, S., Combes, F., Hunt, L. K., et al. 2003, *A&A*, 407, 485
- Gebhardt, K., Bender, R., Bower, G., et al. 2000, *ApJ*, 539, L13
- Gelman, A., Carlin, J. B., Stern, H. S., et al. 2013, *Bayesian Data Analysis*
- Ghosh, K. K., Swartz, D. A., Tennant, A. F., Wu, K., & Saripalli, L. 2005, *ApJ*, 623, 815
- Gil de Paz, A., Boissier, S., Madore, B. F., et al. 2007, *ApJS*, 173, 185
- Gourgoulhon, E., Chamaraux, P., & Fouque, P. 1992, *A&A*, 255, 69
- Graham, A. W. 2012, *ApJ*, 746, 113

- . 2013, *Elliptical and Disk Galaxy Structure and Modern Scaling Laws*, ed. T. D. Oswalt & W. C. Keel, 91
- Graham, A. W. 2016, in *Astrophysics and Space Science Library*, Vol. 418, *Galactic Bulges*, ed. E. Laurikainen, R. Peletier, & D. Gadotti, 263
- Graham, A. W., Dullo, B. T., & Savorgnan, G. A. D. 2015, *ApJ*, 804, 32
- Graham, A. W., Erwin, P., Caon, N., & Trujillo, I. 2001, *ApJ*, 563, L11
- Graham, A. W., Erwin, P., Trujillo, I., & Asensio Ramos, A. 2003, *AJ*, 125, 2951
- Graham, A. W., & Scott, N. 2013, *ApJ*, 764, 151
- Graham, A. W., & Worley, C. C. 2008, *MNRAS*, 388, 1708
- Greene, J. E., Ho, L. C., & Barth, A. J. 2008, *ApJ*, 688, 159
- Greene, J. E., Peng, C. Y., Kim, M., et al. 2010, *ApJ*, 721, 26
- Greene, J. E., Seth, A., Kim, M., et al. 2016, *ApJ*, 826, L32
- Gültekin, K., Richstone, D. O., Gebhardt, K., et al. 2009, *ApJ*, 698, 198
- Habouzit, M., Genel, S., Somerville, R. S., et al. 2019, *MNRAS*, 484, 4413
- Hägele, G. F., Díaz, Á. I., Cardaci, M. V., Terlevich, E., & Terlevich, R. 2010, *MNRAS*, 402, 1005
- Heckman, T. M., Kauffmann, G., Brinchmann, J., et al. 2004, *ApJ*, 613, 109
- Hilbe, J. M., de Souza, R. S., & Ishida, E. E. O. 2017, *Bayesian Models for Astrophysical Data Using R, JAGS, Python, and Stan*, doi:10.1017/CBO9781316459515
- Hilker, M., & Kissler-Patig, M. 1996, *A&A*, 314, 357
- Ho, L. C. 2005, *ApJ*, 629, 680
- Hopkins, P. F., Cox, T. J., Dutta, S. N., et al. 2009a, *ApJS*, 181, 135
- Hopkins, P. F., & Hernquist, L. 2009, *ApJ*, 694, 599
- Hopkins, P. F., Hernquist, L., Cox, T. J., et al. 2006, *ApJS*, 163, 1
- Hopkins, P. F., Lauer, T. R., Cox, T. J., Hernquist, L., & Kormendy, J. 2009b, *ApJS*, 181, 486
- Hopkins, P. F., & Quataert, E. 2010, *MNRAS*, 407, 1529
- Jahnke, K., & Macciò, A. V. 2011, *ApJ*, 734, 92
- Jardel, J. R., Gebhardt, K., Shen, J., et al. 2011, *ApJ*, 739, 21
- Jeong, H., Yi, S. K., Bureau, M., et al. 2009, *MNRAS*, 398, 2028
- Józsa, G. I. G., Oosterloo, T. A., Morganti, R., Klein, U., & Erben, T. 2009, *A&A*, 494, 489
- Karataeva, G. M., Drozdovsky, I. O., Hagen-Thorn, V. A., et al. 2004, *AJ*, 127, 789
- Kauffmann, G., Heckman, T. M., White, S. D. M., et al. 2003a, *MNRAS*, 341, 54
- Kauffmann, G., Heckman, T. M., Tremonti, C., et al. 2003b, *MNRAS*, 346, 1055
- Kaviraj, S. 2014a, *MNRAS*, 440, 2944
- . 2014b, *MNRAS*, 437, L41
- Kelly, B. C. 2007, *ApJ*, 665, 1489
- Kennedy, R., Bamford, S. P., Häußler, B., et al. 2016, *MNRAS*, 460, 3458
- Khochfar, S., & Burkert, A. 2001, *ApJ*, 561, 517
- Khochfar, S., & Silk, J. 2009, *MNRAS*, 397, 506
- Kim, D.-W., Guhathakurta, P., van Gorkom, J. H., Jura, M., & Knapp, G. R. 1988, *ApJ*, 330, 684
- King, A. 2003, *ApJ*, 596, L27
- Knapen, J. H., Cisternas, M., & Querejeta, M. 2015, *MNRAS*, 454, 1742
- Knapen, J. H., Erroz-Ferrer, S., Roa, J., et al. 2014, *A&A*, 569, A91
- Kormendy, J. 1982, *ApJ*, 257, 75
- Kormendy, J. 1993, in *IAU Symposium*, Vol. 153, *Galactic Bulges*, ed. H. Dejonghe & H. J. Habing, 209
- . 2013, *Secular Evolution in Disk Galaxies*, ed. J. Falcón-Barroso & J. H. Knapen, 1
- Kormendy, J., & Ho, L. C. 2013, *ARA&A*, 51, 511
- Kormendy, J., & Kennicutt, Jr., R. C. 2004, *ARA&A*, 42, 603
- Kormendy, J., & Richstone, D. 1995, *ARA&A*, 33, 581
- Krajnović, D., Cappellari, M., & McDermid, R. M. 2018, *MNRAS*, 473, 5237
- Krajnović, D., Ural, U., Kuntschner, H., et al. 2020, *A&A*, 635, A129
- Lauer, T. R., Faber, S. M., Richstone, D., et al. 2007, *ApJ*, 662, 808
- Laurikainen, E., Salo, H., Buta, R., & Knapen, J. H. 2007, *MNRAS*, 381, 401
- Lee, J. C., Gil de Paz, A., Kennicutt, Jr., R. C., et al. 2011, *ApJS*, 192, 6
- Leitner, S. N. 2012, *ApJ*, 745, 149
- Leonardi, A. J., & Worthey, G. 2000, *ApJ*, 534, 650
- Lutz, D., Sturm, E., Tacconi, L. J., et al. 2008, *ApJ*, 684, 853
- Madau, P., & Dickinson, M. 2014, *ARA&A*, 52, 415
- Magorrian, J., Tremaine, S., Richstone, D., et al. 1998, *AJ*, 115, 2285
- Makarov, D., Prugniel, P., Terekhova, N., Courtois, H., & Vauglin, I. 2014, *A&A*, 570, A13
- Malin, D., & Hadley, B. 1997, *PASA*, 14, 52
- Man, A. W. S., Toft, S., Zirm, A. W., Wuyts, S., & van der Wel, A. 2012, *ApJ*, 744, 85
- Marconi, A., & Hunt, L. K. 2003, *ApJ*, 589, L21
- Marleau, F. R., Noriega-Crespo, A., Misselt, K. A., et al. 2006, *ApJ*, 646, 929
- Martin, D. C., Fanson, J., Schiminovich, D., et al. 2005, *ApJ*, 619, L1
- Martin, G., Kaviraj, S., Volonteri, M., et al. 2018a, *MNRAS*, arXiv:1801.09699
- . 2018b, *MNRAS*, 476, 2801
- Martín-Navarro, I., Brodie, J. P., Romanowsky, A. J., Ruiz-Lara, T., & van de Ven, G. 2018, *Nature*, 553, 307
- McConnell, N. J., & Ma, C.-P. 2013, *ApJ*, 764, 184
- McDermid, R. M., Alatalo, K., Blitz, L., et al. 2015, *MNRAS*, 448, 3484
- McLure, R. J., & Dunlop, J. S. 2002, *MNRAS*, 331, 795
- Meidt, S. E., Schinnerer, E., Knapen, J. H., et al. 2012, *ApJ*, 744, 17
- Merloni, A., Rudnick, G., & Di Matteo, T. 2004, *MNRAS*, 354, L37
- Merritt, D. 2006, *ApJ*, 648, 976
- Möllenhoff, C. 2004, *A&A*, 415, 63
- Möllenhoff, C., Popescu, C. C., & Tuffs, R. J. 2006, *A&A*, 456, 941
- Morrissey, P., Conrow, T., Barlow, T. A., et al. 2007, *ApJS*, 173, 682
- Muñoz-Mateos, J. C., Sheth, K., Regan, M., et al. 2015, *ApJS*, 219, 3
- Mulder, P. S., van Driel, W., & Braine, J. 1995, *A&A*, 300, 687
- Mundy, C. J., Conelice, C. J., Duncan, K. J., et al. 2017, *MNRAS*, 470, 3507
- Murray, N., Quataert, E., & Thompson, T. A. 2005, *ApJ*, 618, 569
- Naab, T., Jesseit, R., & Burkert, A. 2006a, *MNRAS*, 372, 839
- Naab, T., Khochfar, S., & Burkert, A. 2006b, *ApJ*, 636, L81
- Nemmen, R. S., Georganopoulos, M., Guiriec, S., et al. 2012, *Science*, 338, 1445
- Netzer, H. 2009, *MNRAS*, 399, 1907
- Nguyen, D. D., Seth, A. C., Neumayer, N., et al. 2019, *ApJ*, 872, 104
- Nolan, L. A., Raychaudhury, S., & Kabán, A. 2007, *MNRAS*, 375, 381
- Nowak, N., Thomas, J., Erwin, P., et al. 2010, *MNRAS*, 403, 646
- O’Connell, R. W. 1999, *ARA&A*, 37, 603
- O’Dea, C. P., Baum, S. A., Privon, G., et al. 2008, *ApJ*, 681, 1035
- Pannella, M., Carilli, C. L., Daddi, E., et al. 2009, *ApJ*, 698, L116
- Paturel, G., Petit, C., Prugniel, P., et al. 2003, *A&A*, 412, 45
- Peng, C. Y. 2007, *ApJ*, 671, 1098
- Pérez-González, P. G., Rieke, G. H., Villar, V., et al. 2008, *ApJ*, 675, 234
- Peterson, B. M. 1993, *PASP*, 105, 247
- Peterson, B. M., Bentz, M. C., Desroches, L.-B., et al. 2005, *ApJ*, 632, 799
- Rampazzo, R., Marino, A., Tantaló, R., et al. 2007, *MNRAS*, 381, 245
- Richstone, D., Ajhar, E. A., Bender, R., et al. 1998, *Nature*, 395, A14
- Rodríguez-Gomez, V., Genel, S., Vogelsberger, M., et al. 2015, *MNRAS*, 449, 49
- Rodríguez-Gomez, V., Pillepich, A., Sales, L. V., et al. 2016, *MNRAS*, 458, 2371
- Rosario, D. J., Santini, P., Lutz, D., et al. 2012, *A&A*, 545, A45
- Russell, H. R., McNamara, B. R., Edge, A. C., et al. 2014, *ApJ*, 784, 78

- Russell, H. R., McNamara, B. R., Fabian, A. C., et al. 2019, arXiv e-prints, arXiv:1902.09227
- Saglia, R. P., Opitsch, M., Erwin, P., et al. 2016, ApJ, 818, 47
- Sahu, N., Graham, A. W., & Davis, B. L. 2019, arXiv e-prints, arXiv:1903.04738
- Salo, H., Laurikainen, E., Laine, J., et al. 2015, ApJS, 219, 4
- Salomé, P., & Combes, F. 2003, A&A, 412, 657
- Sandage, A. 1961, The Hubble Atlas of Galaxies
- Sanders, D. B., Soifer, B. T., Elias, J. H., et al. 1988, ApJ, 325, 74
- Savorgnan, G. A. D., & Graham, A. W. 2016, ApJS, 222, 10
- Savorgnan, G. A. D., Graham, A. W., Marconi, A., & Sani, E. 2016, ApJ, 817, 21
- Schawinski, K., Khochfar, S., Kaviraj, S., et al. 2006, Nature, 442, 888
- Schawinski, K., Urry, C. M., Virani, S., et al. 2010, ApJ, 711, 284
- Schawinski, K., Urry, C. M., Simmons, B. D., et al. 2014, MNRAS, 440, 889
- Schechter, P. L., & Gunn, J. E. 1978, AJ, 83, 1360
- Schinnerer, E., & Scoville, N. 2002, ApJ, 577, L103
- Schlegel, D. J., Finkbeiner, D. P., & Davis, M. 1998, ApJ, 500, 525
- Schweizer, F. 1987, in IAU Symposium, Vol. 127, Structure and Dynamics of Elliptical Galaxies, ed. P. T. de Zeeuw, 109–122
- Segers, M. C., Schaye, J., Bower, R. G., et al. 2016, MNRAS, 461, L102
- Sérsic, J. L. 1968, Atlas de Galaxias Australes
- Shane, W. W. 1980, A&A, 82, 314
- Shankar, F., Weinberg, D. H., & Miralda-Escudé, J. 2009, ApJ, 690, 20
- Sheth, K., Regan, M., Hinz, J. L., et al. 2010, PASP, 122, 1397
- Sijacki, D., Vogelsberger, M., Genel, S., et al. 2015, MNRAS, 452, 575
- Sil'chenko, O. K., Moiseev, A. V., Afanasiev, V. L., Chavushyan, V. H., & Valdes, J. R. 2003, ApJ, 591, 185
- Silk, J., & Rees, M. J. 1998, A&A, 331, L1
- Simmons, B. D., Smethurst, R. J., & Lintott, C. 2017, MNRAS, 470, 1559
- Simmons, B. D., Lintott, C., Schawinski, K., et al. 2013, MNRAS, 429, 2199
- Smith, D. A., Neff, S. G., Bothun, G. D., et al. 1996, ApJ, 473, L21
- Smith, R. J., & Edge, A. C. 2017, MNRAS, 471, L66
- Spitler, L. R., Forbes, D. A., & Beasley, M. A. 2008, MNRAS, 389, 1150
- Springel, V., White, S. D. M., Jenkins, A., et al. 2005, Nature, 435, 629
- Steinmetz, M., & Navarro, J. F. 2002, NewA, 7, 155
- Struve, C., Oosterloo, T., Sancisi, R., Morganti, R., & Emonts, B. H. C. 2010, A&A, 523, A75
- Terrazas, B. A., Bell, E. F., Woo, J., & Henriques, B. M. B. 2017, ApJ, 844, 170
- Thomas, D., Maraston, C., Bender, R., & Mendes de Oliveira, C. 2005, ApJ, 621, 673
- Thomas, D., Maraston, C., Schawinski, K., Sarzi, M., & Silk, J. 2010, MNRAS, 404, 1775
- Toba, Y., Nagao, T., Wang, W.-H., et al. 2017, ApJ, 840, 21
- Tonini, C., Mutch, S. J., Croton, D. J., & Wyithe, J. S. B. 2016, MNRAS, 459, 4109
- Toomre, A., & Toomre, J. 1972, ApJ, 178, 623
- Treuthardt, P., Buta, R., Salo, H., & Laurikainen, E. 2007, AJ, 134, 1195
- van den Bosch, R. C. E. 2016, ApJ, 831, 134
- van Driel, W., & Buta, R. 1993, PASJ, 45, L47
- van Son, L. A. C., Barber, C., Bahé, Y. M., et al. 2019, MNRAS, arXiv:1901.03156
- Visvanathan, N., & Griersmith, D. 1977, A&A, 59, 317
- Watkins, A. E., Mihos, J. C., Harding, P., & Feldmeier, J. J. 2014, ApJ, 791, 38
- Watson, D. M., Guptill, M. T., & Buchholz, L. M. 1994, ApJ, 420, L21
- Wehner, E. H., Gallagher, J. S., Papaderos, P., Fritze-von Alvensleben, U., & Westfall, K. B. 2006, MNRAS, 371, 1047
- Wehner, E. H., & Gallagher, III, J. S. 2005, ApJ, 618, L21
- Weinberger, R., Springel, V., Hernquist, L., et al. 2017, MNRAS, 465, 3291
- White, S. D. M., & Rees, M. J. 1978, MNRAS, 183, 341
- Wild, V., Heckman, T., & Charlot, S. 2010, MNRAS, 405, 933
- Yang, G., Chen, C.-T. J., Vito, F., et al. 2017, ApJ, 842, 72
- Yi, S. K., Lee, J., Sheen, Y.-K., et al. 2011, ApJS, 195, 22
- Young, L. M., Bureau, M., Davis, T. A., et al. 2011, MNRAS, 414, 940
- Zubovas, K., & King, A. R. 2012, MNRAS, 426, 2751

7. APPENDIX

A. APPENDIX A

A.1. Bayesian approach

We have performed linear regression fits to the $(M_{\text{BH}}, \mathcal{C}_{\text{UV,tot}})$ dataset applying a Bayesian statistical inference with Markov Chain Monte Carlo (MCMC) technique¹¹. The regression fits take into account errors in M_{BH} and $\mathcal{C}_{\text{UV,tot}}$ and an additional spread not explained by the error bars. The MCMC runs were implemented in our work through the Stan programming language¹² (e.g., Carpenter et al. 2017). In addition to the slope, intercept, and dispersion, the model parameters include ‘true’ color and SMBH mass values. In our implementation, the observed SMBH mass upper limits were modeled by drawing samples from an asymmetric normal distribution centered around the true values with standard deviation having an upper wing which equals to the error bar of the measurements and a lower wing with a much larger size. As such, the regression fits probe a large range in SMBH masses for galaxies with SMBH upper limits. For the Bayesian analysis, we used non-informative prior distributions (e.g., Gelman et al. 2013) and checked that the results did not depend on the choice of the prior details.

Fig. 7 shows the results of the Bayesian linear regressions. The shaded regions indicate the 95% Highest Density Interval (HDI) for the derived fits. Note that the HDIs are not symmetric, since the derived parameters exhibit skewed posterior distributions. The dotted lines mark the 1σ and 3σ intervals for the additional real dispersion that is not explained by the error bars (Fig. 7). The probability distribution functions for these additional dispersions are not symmetrical, and the derived values exhibit 95% HDIs of (0.00, 0.74) and (0.14, 0.68) for the early- and late-type galaxies. For the former, the additional dispersion is not significantly different from zero, therefore, the observed dispersion could be fully explained by the error bars. In contrast, an additional real dispersion is needed for the latter to explain the residuals from the fitted relation.

In Fig. 8, we show the probability distribution functions (PDF) for the disparity in slope between early- and late-type $M_{\text{BH}} - \mathcal{C}_{\text{UV,tot}}$ relations obtained by applying the linear Bayesian regression fits. The PDFs are determined using all the individual steps of the computed chains, thus avoiding any assumption about the probability distribution of the

¹¹ Interested readers are referred to Andreon & Weaver (2015, page 134) and Hilbe et al. (2017, page 278) for a description of the MCMC method.

¹² <https://mc-stan.org>

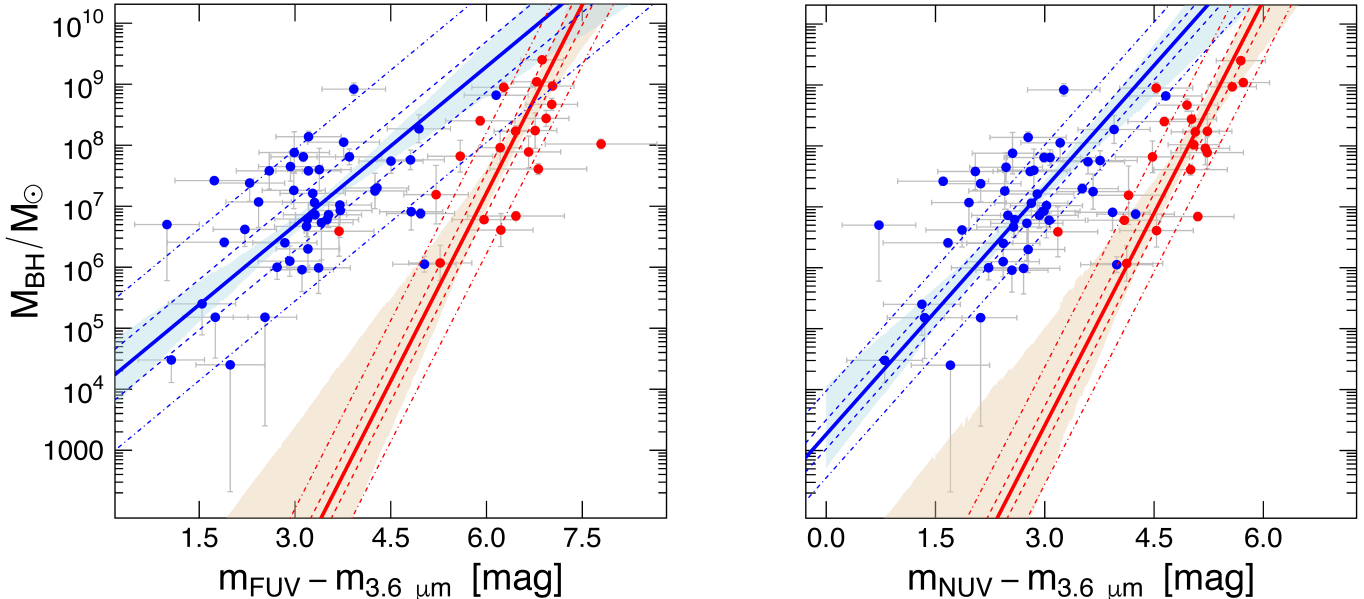


FIG. 7.— Similar to Fig. 2, but here plotting the results of our symmetric linear Bayesian regression analysis. Early-type and late-type galaxies are shown in red and blue, respectively. The shaded regions indicate the 95% Highest Density Interval for the derived fits. The dotted lines mark the 1σ and 3σ intervals for the additional real dispersion not explained by the error bars, see the text for further detail.

derived parameters. We find that the significance levels for rejecting the null hypothesis of both morphological types having the same slope are 1.7% and 6.7% for the FUV and NUV relations, respectively.

B. APPENDIX B

B.1. *Outliers in the $M_{\text{BH}} - \mathcal{C}_{\text{UV,tot}}$ diagrams*

Five galaxies in our sample, which offset notably from the $M_{\text{BH}} - \mathcal{C}$ relations (Fig. 2).

B.1.1. *NGC 2685*

The Helix Galaxy NGC 2685 is a well-studied polar ring lenticular galaxy (Schechter & Gunn 1978, Shane 1980; Watson et al. 1994; Eskridge & Pogge 1997, Karataeva et al. 2004; Schinnerer & Scoville 2002; Rampazzo et al. 2007; Józsa et al. 2009). Sandage (1961) referred to it as to the most unusual of all the galaxies in his atlas, and subsequent studies confirmed its rare nature (e.g., Eskridge & Pogge 1997; Schinnerer & Scoville 2002; Józsa et al. 2009). The galaxy contains a large concentration of molecular, neutral and atomic hydrogen gas in its polar ring. Fig. 2 shows it resides in the $M_{\text{BH}} - \mathcal{C}$ blue sequence defined by late-type galaxies and its $\mathcal{C}_{\text{UV,tot}}$ color is abnormally ($\sim 1.90/1.00$ FUV/NUV mag) bluer than that predicted for early-type galaxies given the galaxy’s SMBH mass. This result agrees with the two formation scenarios considered in the literature for NGC 2685: formation via accretion of a small gas-rich companion (e.g., Shane 1980; Watson et al. 1994; Schinnerer & Scoville 2002) and a merger of two disk galaxies (e.g., Józsa et al. 2009).

B.1.2. *NGC 3310*

The starburst galaxy NGC 3310 is a well-studied peculiar spiral galaxy (SAB) known for its very blue color, circumnuclear ring of star formation, tidal features and very bright infrared luminosity (e.g., Balick & Heckman 1981; Mulder et al. 1995; Smith et al. 1996; Conselice et al. 2000; Elmegreen et al. 2002; Wehner & Gallagher 2005; Wehner et al. 2006; Hägele et al. 2010). The favored scenario for the formation of the galaxy is through accretion of a small gas-rich dwarf galaxy ~ 10 Myr ago (Balick & Heckman 1981; Mulder et al. 1995; Smith et al. 1996; Conselice et al. 2000; Wehner & Gallagher 2005; Wehner et al. 2006). Consistent with this picture, Fig. 2 shows that the galaxy’s $\mathcal{C}_{\text{UV,tot}}$ color is ($\sim 1.99/1.79$ FUV/NUV mag) bluer than expected for late-type galaxies.

B.1.3. *NGC 3368*

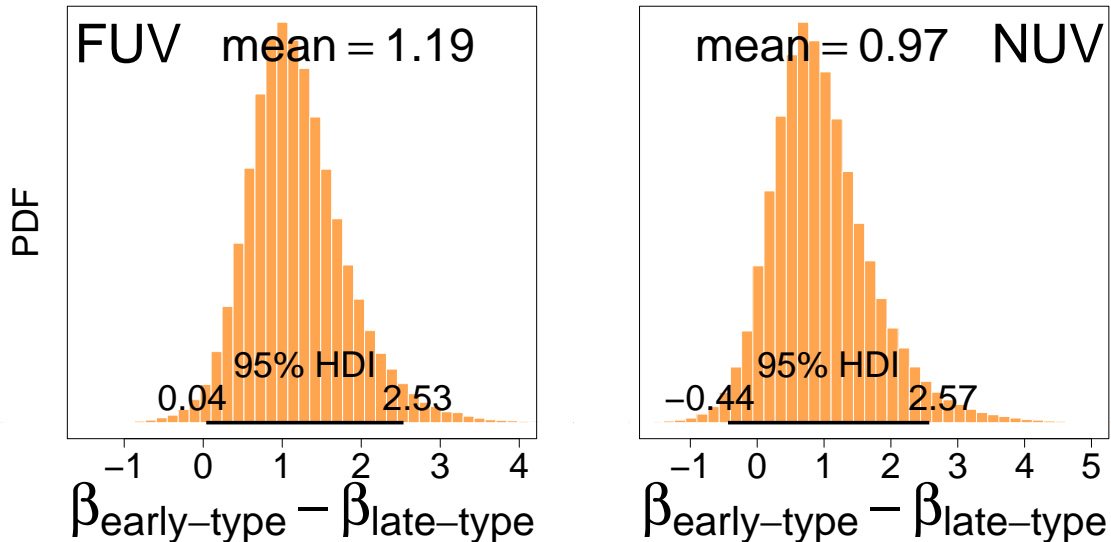


FIG. 8.— probability distribution function (PDF) for the difference in slopes (β) between the linear Bayesian regression fits to the early- and late-type ($M_{\text{BH}}, C_{\text{UV,tot}}$) data (see Fig. 7).

The case of the double-barred spiral (SAB) galaxy NGC 3368 is less clear. It is the brightest galaxy in the nearby NGC 3368 group (Sil'chenko et al. 2003; Watkins et al. 2014), containing a dominant pseudo-bulge, a small classical bulge and box/peanut component (Nowak et al. 2010; Erwin et al. 2015). Not only its $C_{\text{UV,tot}}$ color is ($\sim 1.81/1.61$ FUV/NUV mag) redder than that expected for late-type galaxies given its M_{BH} , the galaxy also falls on the $M_{\text{BH}} - C_{\text{NUV,tot}}$ red sequence defined by early-type galaxies (Fig. 2). Fig. 2 shows that NGC 3368 lies 0.45 dex below the best-fitting $M_{\text{BH}} - \sigma$ line in the $\log M_{\text{BH}}$ direction, this might suggest that the galaxy has abnormally low SMBH mass, rather than a discrepant redder color. We cannot rule out the possibility where both the black hole mass and color conspire, causing the offset in the $M_{\text{BH}} - C$ diagrams (Fig. 2).

B.1.4. NGC 4826

The SABa galaxy NGC 4826 is also referred to as the Evil- or Black-Eye Galaxy, attributed to its dusty disk with a radius $R \sim 50''$. It has a large-scale counter-rotating gas disk (van Driel & Buta 1993; Braun et al. 1994; García-Burillo et al. 2003). The galaxy is the most significant outlier in the $M_{\text{BH}} - C_{\text{UV,tot}}$ diagrams, having $C_{\text{UV,tot}}$ color ($\sim 2.68/2.04$ FUV/NUV mag) redder than what is expected for late-type galaxies (Fig. 2). The dust disk likely explains the deviant (redder) UV–[3.6] color for the galaxy. Fig. 2 shows that the galaxy falls on the red, early-type sequence, despite being a late-type galaxy.

B.1.5. NGC 5018

The giant elliptical (E3) NGC 5018 is the most intriguing case. It is the brightest member of the poor NGC 5018 group containing 5 galaxies (Gourgoulhon et al. 1992) known for its morphological peculiarity including shells, ripples and dust lane (Schweizer 1987; Kim et al. 1988; Malin & Hadley 1997; Leonardi & Worthey 2000; Knapen et al. 2014). There is a tidal bridge between NGC 5018 and a gas-rich spiral companion NGC 5022, detected in optical (Schweizer 1987; Malin & Hadley 1997) and HI observations (Kim et al. 1988; Ghosh et al. 2005), which was built up via accretion of gaseous material from NGC 5022 onto NGC 5018. NGC 5018 is currently forming stars (Ghosh et al. 2005) and about 12 % (by mass) of the stars in the galaxy are younger than 3.4 Gyr (Nolan et al. 2007, see also Leonardi & Worthey 2000). The galaxy has low metallicity and far- and mid-UV flux deficits unusual for its luminosity and velocity dispersion (Bertola et al. 1993; Buson et al. 2004). While Carollo & Danziger (1994) attributed the observed unusual metallicity and UV fluxes to nuclear dust extinction, the galaxy is an outlier from the $C_{\text{FUV,tot}} - M_{\text{BH}}$ diagram but not $C_{\text{NUV,tot}} - M_{\text{BH}}$ diagram (Fig. 2), revealing that the offset nature of the galaxy is not because of dust extinction but rather owing to the mixing of young and old populations of stars at the galaxy center washing out pre-existing metallicity (Bertola et al. 1993; Hilker & Kissler-Patig 1996; Kim et al. 1988; Buson et al. 2004). We also note that the galaxy offsets slightly from the $M_{\text{BH}} - L_{3.6,\text{tot}}$ relation towards a brighter magnitude, this may partly explain the deviant red color of the galaxy.

C. APPENDIX C

Table 5 presents total magnitudes, bulge-to-total (B/T) and disk-to-total (D/T) ratios, dust corrections and SMBH masses for our sample galaxies.

D. APPENDIX D

We use our $M_{\text{BH}} - C_{\text{FUV,tot}}$ and $M_{\text{BH}} - C_{\text{NUV,tot}}$ relations (Table 1) together with the appropriate asymptotic galaxy colors derived based on the asymptotic FUV, NUV and $3.6 \mu\text{m}$ magnitudes from Bouquin et al. (2018, their Table 1) to predict tentative BH masses in a sample of 1382 *GALEX*/*S*⁴G galaxies with no measured BH masses (Table 6). From the Bouquin et al. (2018) sample, we excluded galaxies that are: highly inclined, dust obscured and with prominent large-scale bars and rings. In contrast to the total (B+D) magnitudes in this paper (Table 5), the Bouquin et al. (2018) asymptotic magnitudes, which were not corrected for internal dust attenuation, contain additional fluxes from bars, rings and nuclear components as such we caution about overinterpreting these predicted BH masses. Furthermore, *Chandra* X-ray data or/and high-resolution radio data are important to confirm the presence of a central black hole in the low-mass ($M_* \lesssim 10^{10} M_{\odot}$) *GALEX*/*S*⁴G galaxies.

TABLE 5
 BASIC DATA FOR OUR SAMPLE OF 67 *GALEX*/S⁴G GALAXIES WITH DIRECTLY MEASURED SUPERMASSIVE BLACK HOLE MASSES

Galaxy	Type	m_{FUV} B+D	m_{NUV} B+D	$m_{3.6}$ B+D	B/T FUV/NUV	B/T 3.6	D/T FUV/NUV	D/T 3.6	Dust _{corr} (B and D) _{3.6}	Dust _{corr} (B and D) _{FUV}	Dust _{corr} (B and D) _{NUV}	log M_{BH} [M_{\odot}]
(1)	(2)	(3)	(4)	(5)	(6)	(7)	(8)	(9)	(10)	(11)	(12)	(13)
NGC 0289	SBbc	12.84 ^{+0.39} _{-0.39}	12.67 ^{+0.40} _{-0.40}	10.55 ^{+0.38} _{-0.38}	—	0.02	0.92	0.92	0.14/0.05	—/0.66	—/0.66	7.38 ^{+0.30} _{-0.37}
NGC 0428	SABm	12.91 ^{+0.37} _{-0.37}	12.65 ^{+0.37} _{-0.37}	11.85 ^{+0.35} _{-0.35}	—	0.00	0.93	0.93	0.13/0.05	—/0.70	—/0.70	4.48 ^{+0.35} _{-4.48}
NGC 0613	SBbc	12.99 ^{+0.36} _{-0.36}	12.46 ^{+0.36} _{-0.36}	9.61 ^{+0.34} _{-0.34}	0.04	0.13	0.92	0.75	0.13/0.05	1.29/0.62	1.29/0.62	7.60 ^{+0.35} _{-0.35}
NGC 1042	SABc	13.08 ^{+0.39} _{-0.39}	12.80 ^{+0.39} _{-0.39}	11.10 ^{+0.37} _{-0.37}	—	0.02	0.97	0.97	0.13/0.05	—/0.70	—/0.70	4.40 ^{+2.08} _{-4.40}
NGC 1052	E4	16.81 ^{+0.24} _{-0.24}	15.28 ^{+0.24} _{-0.24}	10.05 ^{+0.23} _{-0.23}	0.67	0.72	—	—	0.01/—	0.23/—	0.23/—	8.24 ^{+0.29} _{-0.29}
NGC 1097	SBb	12.10 ^{+0.37} _{-0.37}	11.66 ^{+0.37} _{-0.37}	8.89 ^{+0.35} _{-0.35}	0.11	0.22	0.79	0.56	0.15/0.05	1.41/0.73	1.41/0.73	8.14 ^{+0.09} _{-0.09}
NGC 1300	SBc	13.21 ^{+0.40} _{-0.40}	12.78 ^{+0.40} _{-0.40}	10.23 ^{+0.38} _{-0.38}	—	0.07	0.87	0.87	0.16/0.05	—/0.76	—/0.76	7.88 ^{+0.34} _{-0.34}
NGC 1386	SB0-a	15.79 ^{+0.35} _{-0.35}	14.64 ^{+0.36} _{-0.36}	10.51 ^{+0.32} _{-0.32}	0.26	0.36	0.70	0.58	0.32/0.10	1.54/1.00	1.54/1.00	6.07 ^{+0.29} _{-0.29}
NGC 1493	SBc	12.99 ^{+0.40} _{-0.40}	12.76 ^{+0.38} _{-0.38}	11.45 ^{+0.36} _{-0.36}	—	0.00	0.97	0.97	0.11/0.04	—/0.53	—/0.53	5.40 ^{+0.51} _{-5.40}
NGC 2685	SB0-a	14.66 ^{+0.39} _{-0.39}	14.15 ^{+0.39} _{-0.39}	10.97 ^{+0.36} _{-0.36}	0.36	0.46	0.54	0.41	0.23/0.08	1.82/1.17	1.83/1.18	6.59 ^{+0.41} _{-6.59}
NGC 2748	Sbc	13.98 ^{+0.36} _{-0.36}	13.52 ^{+0.36} _{-0.36}	11.05 ^{+0.34} _{-0.34}	—	0.03	0.97	0.97	0.34/0.11	—/1.16	—/1.17	7.65 ^{+0.24} _{-0.24}
NGC 2787	SB0-a	16.66 ^{+0.54} _{-0.54}	14.85 ^{+0.36} _{-0.36}	9.85 ^{+0.35} _{-0.35}	0.39	0.51	0.59	0.45	0.19/0.07	2.32/1.65	2.34/1.66	7.61 ^{+0.09} _{-0.09}
NGC 2903	SBbc	11.66 ^{+0.33} _{-0.33}	11.17 ^{+0.36} _{-0.36}	8.35 ^{+0.34} _{-0.34}	—	0.07	0.90	0.90	0.25/0.08	—/0.96	—/0.96	7.06 ^{+0.28} _{-7.06}
NGC 2964	SBbc	14.13 ^{+0.35} _{-0.35}	13.47 ^{+0.35} _{-0.35}	10.72 ^{+0.34} _{-0.34}	—	0.10	0.90	0.90	0.20/0.06	—/0.75	—/0.75	6.73 ^{+0.61} _{-6.73}
NGC 2974	E4	16.98 ^{+0.23} _{-0.23}	15.59 ^{+0.24} _{-0.24}	10.52 ^{+0.22} _{-0.22}	0.49	0.54	—	—	0.01/—	0.44/—	0.45/0.45	8.23 ^{+0.09} _{-0.09}
NGC 3021	Sbc	14.60 ^{+0.35} _{-0.35}	14.07 ^{+0.35} _{-0.35}	11.62 ^{+0.34} _{-0.34}	—	0.01	0.98	0.98	0.19/0.06	—/0.71	—/0.71	7.26 ^{+0.30} _{-0.30}
NGC 3031	Sab	10.07 ^{+0.36} _{-0.36}	9.29 ^{+0.45} _{-0.45}	6.22 ^{+0.39} _{-0.39}	0.14	0.46	0.86	0.54	0.23/0.08	1.96/1.30	1.97/1.31	7.81 ^{+0.13} _{-0.13}
NGC 3079	SBc	12.10 ^{+0.36} _{-0.36}	11.69 ^{+0.36} _{-0.36}	9.26 ^{+0.34} _{-0.34}	0.07	0.24	0.93	0.77	0.57/0.24	1.81/1.73	1.82/1.73	6.40 ^{+0.05} _{-0.05}
NGC 3115	E-S0	14.45 ^{+0.36} _{-0.36}	12.71 ^{+0.35} _{-0.35}	8.18 ^{+0.33} _{-0.33}	0.63	0.74	0.37	0.26	0.36/0.13	1.86/1.37	1.87/1.38	8.95 ^{+0.09} _{-0.09}
NGC 3310	SBbc	11.68 ^{+0.36} _{-0.36}	11.41 ^{+0.36} _{-0.36}	10.69 ^{+0.34} _{-0.34}	0.16	0.33	0.83	0.63	0.13/0.05	1.33/0.65	1.33/0.66	6.70 ^{+0.92} _{-6.70}
NGC 3368	SBab	13.76 ^{+0.38} _{-0.38}	13.04 ^{+0.38} _{-0.38}	8.79 ^{+0.36} _{-0.36}	—	0.07	0.92	0.92	0.15/0.05	—/0.71	—/0.71	6.88 ^{+0.08} _{-0.08}
NGC 3414	SB0	16.39 ^{+0.39} _{-0.39}	15.13 ^{+0.38} _{-0.38}	10.49 ^{+0.34} _{-0.34}	0.57	0.69	0.41	0.29	0.13/0.05	1.36/0.69	1.37/0.69	8.40 ^{+0.07} _{-0.07}
NGC 3423	Sc	12.92 ^{+0.37} _{-0.37}	12.52 ^{+0.37} _{-0.37}	11.17 ^{+0.35} _{-0.35}	—	0.06	0.95	0.95	0.12/0.05	—/0.71	—/0.71	5.18 ^{+0.67} _{-5.18}
NGC 3489	SB0-a	16.01 ^{+0.36} _{-0.36}	14.14 ^{+0.36} _{-0.36}	10.05 ^{+0.33} _{-0.33}	0.23	0.32	0.71	0.58	0.19/0.06	1.38/0.71	1.39/0.71	6.78 ^{+0.05} _{-0.05}
NGC 3608	E2	17.58 ^{+0.29} _{-0.29}	15.51 ^{+0.29} _{-0.29}	10.56 ^{+0.27} _{-0.27}	1.00	1.00	—	—	0.01/—	0.17/—	0.18/—	8.67 ^{+0.10} _{-0.10}
NGC 3627	SBb	12.07 ^{+0.35} _{-0.35}	11.35 ^{+0.35} _{-0.35}	8.36 ^{+0.34} _{-0.34}	0.03	0.12	0.93	0.78	0.26/0.08	1.62/1.00	1.62/1.00	6.93 ^{+0.05} _{-0.05}
NGC 3642	Sbc	13.25 ^{+0.44} _{-0.44}	13.12 ^{+0.39} _{-0.39}	11.51 ^{+0.42} _{-0.42}	0.03	0.14	0.95	0.80	0.12/0.042	1.21/0.55	1.21/0.55	7.42 ^{+0.04} _{-7.42}
NGC 4041	Sbc	13.45 ^{+0.36} _{-0.36}	12.96 ^{+0.36} _{-0.36}	10.73 ^{+0.35} _{-0.35}	0.03	0.14	0.95	0.80	0.12/0.04	1.28/0.61	1.28/0.61	6.00 ^{+0.20} _{-6.00}
NGC 4051	SABb	12.89 ^{+0.36} _{-0.36}	12.40 ^{+0.36} _{-0.36}	9.97 ^{+0.34} _{-0.34}	0.03	0.15	0.96	0.80	0.13/0.04	1.26/0.59	1.27/0.59	6.10 ^{+0.25} _{-0.25}
NGC 4088	SABc	12.92 ^{+0.37} _{-0.37}	12.31 ^{+0.37} _{-0.37}	9.72 ^{+0.35} _{-0.35}	—	0.02	0.98	0.98	0.32/0.11	—/1.08	—/1.08	6.79 ^{+0.29} _{-6.79}
NGC 4151	SBab	13.16 ^{+0.36} _{-0.36}	13.02 ^{+0.36} _{-0.36}	10.03 ^{+0.35} _{-0.35}	0.22	0.44	0.78	0.56	0.14/0.05	1.39/0.71	1.39/0.71	7.81 ^{+0.08} _{-0.08}
NGC 4203	E-S0	15.55 ^{+0.37} _{-0.37}	14.44 ^{+0.36} _{-0.36}	9.96 ^{+0.35} _{-0.35}	1.0	1.0	—	—	0.11/0.04	1.20/—	1.20/—	7.82 ^{+0.26} _{-0.26}
NGC 4212	Sc	14.08 ^{+0.36} _{-0.36}	13.42 ^{+0.36} _{-0.36}	10.71 ^{+0.34} _{-0.34}	—	0.04	0.96	0.96	0.18/0.06	—/0.82	—/0.82	5.99 ^{+0.42} _{-5.99}
NGC 4245	SB0-a	16.20 ^{+0.36} _{-0.36}	15.14 ^{+0.37} _{-0.37}	10.99 ^{+0.34} _{-0.34}	0.11	0.18	0.82	0.70	0.13/0.05	1.32/0.64	1.32/0.64	7.19 ^{+0.48} _{-7.19}

Notes.—Col. (1) galaxy name. Col. (2) morphological type from HyperLeda, in good agreement with the classification in NED. Cols. (3)-(5) dust-corrected, FUV, NUV and 3.6 μm total ($B+D$) apparent magnitudes (m_{FUV} , m_{NUV} and $m_{3.6}$). Cols. (6)-(9) FUV, NUV and 3.6 μm bulge-to-total (B/T) and disk-to-total (D/T) ratios. Cols. (10)-(12) bulge and disk dust corrections in $m_{3.6}$, FUV- and NUV-bands, see Section 3.1. Col. (13) supermassive black hole mass from van den Bosch (2016).

TABLE 5
(Continued)

Galaxy	Type	m_{FUV} B+D	m_{NUV} B+D	$m_{3.6}$ B+D	B/T FUV/NUV	B/T 3.6	D/T FUV/NUV	D/T 3.6	Dust _{corr} (B and D) _{3.6}	Dust _{corr} (B and D) _{FUV}	Dust _{corr} (B and D) _{NUV}	log M_{BH} [M_{\odot}] (13)
(1)	(2)	(3)	(4)	(5)	(6)	(7)	(8)	(9)	(10)	(11)	(12)	(13)
NGC 4258	SBbc	11.10 ^{+0.36} _{-0.36}	10.69 ^{+0.36} _{-0.36}	7.89 ^{+0.35} _{-0.35}	—	0.07	0.96	0.96	0.32/0.10	—/1.02	—/1.02	7.58 ^{+0.03} _{-0.03}
NGC 4278	E1-2	16.00 ^{+0.24} _{-0.24}	14.99 ^{+0.24} _{-0.24}	9.79 ^{+0.22} _{-0.22}	0.65	0.71	—	—	0.01/—	0.25/—	0.26/—	7.96 ^{+0.27} _{-0.27}
NGC 4314	SBa	15.16 ^{+0.35} _{-0.35}	14.27 ^{+0.35} _{-0.35}	10.34 ^{+0.34} _{-0.34}	0.08	0.17	0.79	0.57	0.12/0.05	1.32/0.67	1.33/0.67	6.91 ^{+0.30} _{-6.91}
NGC 4321	SABb	12.17 ^{+0.36} _{-0.36}	11.56 ^{+0.36} _{-0.36}	8.99 ^{+0.34} _{-0.34}	—	0.10	0.90	0.90	0.12/0.05	—/0.67	—/0.67	6.67 ^{+0.17} _{-6.67}
NGC 4371	SB0-a	16.90 ^{+0.54} _{-0.54}	15.54 ^{+0.36} _{-0.36}	10.44 ^{+0.32} _{-0.32}	0.16	0.23	0.74	0.62	0.12/0.05	1.41/0.76	1.41/0.76	6.84 ^{+0.07} _{-6.84}
NGC 4374	E1	15.77 ^{+0.24} _{-0.24}	14.31 ^{+0.23} _{-0.23}	8.74 ^{+0.22} _{-0.22}	0.60	0.65	—	—	0.01/—	0.35/—	0.35/—	8.97 ^{+0.05} _{-0.05}
NGC 4388	SBb	13.42 ^{+0.35} _{-0.35}	12.60 ^{+0.36} _{-0.36}	10.11 ^{+0.34} _{-0.34}	0.06	0.16	0.94	0.84	0.56/0.24	1.97/1.84	1.97/1.85	6.86 ^{+0.04} _{-0.04}
NGC 4472	E2	14.78 ^{+0.21} _{-0.21}	13.60 ^{+0.22} _{-0.22}	7.91 ^{+0.20} _{-0.20}	0.58	0.63	—	—	0.01/—	0.19/—	0.19/—	9.40 ^{+0.04} _{-0.04}
NGC 4501	Sb	13.04 ^{+0.35} _{-0.35}	12.27 ^{+0.35} _{-0.35}	8.76 ^{+0.39} _{-0.39}	—	0.06	0.94	0.94	0.21/0.07	—/0.92	—/0.93	7.30 ^{+0.08} _{-0.08}
NGC 4548	SBb	14.07 ^{+0.37} _{-0.37}	13.48 ^{+0.36} _{-0.36}	9.82 ^{+0.35} _{-0.35}	0.03	0.12	0.93	0.78	0.13/0.05	1.45/0.78	1.46/0.79	7.25 ^{+0.29} _{-0.29}
NGC 4593	SBb	14.26 ^{+0.37} _{-0.37}	13.66 ^{+0.38} _{-0.38}	10.74 ^{+0.36} _{-0.36}	0.10	0.16	0.81	0.61	0.13/0.05	1.36/0.69	1.37/0.69	6.86 ^{+0.21} _{-0.21}
NGC 4594	Sa	13.35 ^{+0.36} _{-0.36}	11.86 ^{+0.37} _{-0.37}	7.20 ^{+0.35} _{-0.35}	0.49	0.83	0.51	0.17	0.31/0.10	1.84/1.27	1.84/1.28	8.82 ^{+0.05} _{-0.05}
NGC 4596	SB0-a	16.72 ^{+0.36} _{-0.36}	15.29 ^{+0.35} _{-0.35}	10.06 ^{+0.32} _{-0.32}	0.13	0.19	0.77	0.65	0.13/0.05	1.32/0.64	1.32/0.65	7.89 ^{+0.26} _{-0.26}
NGC 4698	Sab	14.89 ^{+0.38} _{-0.38}	13.84 ^{+0.36} _{-0.36}	10.08 ^{+0.35} _{-0.35}	0.22	0.44	0.78	0.56	0.17/0.05	1.43/0.74	1.43/0.75	7.76 ^{+0.16} _{-0.16}
NGC 4736	Sab	11.51 ^{+0.36} _{-0.36}	11.07 ^{+0.36} _{-0.36}	8.01 ^{+0.34} _{-0.34}	0.24	0.42	0.54	0.21	0.12/0.04	1.27/0.61	1.28/0.61	6.78 ^{+0.12} _{-0.12}
NGC 4800	Sb	14.64 ^{+0.34} _{-0.34}	13.96 ^{+0.35} _{-0.35}	10.94 ^{+0.34} _{-0.34}	0.04	0.17	0.95	0.80	0.13/0.05	1.28/0.60	1.28/0.61	7.02 ^{+0.13} _{-0.13}
NGC 4826	SABa	12.94 ^{+0.36} _{-0.36}	11.90 ^{+0.36} _{-0.36}	7.91 ^{+0.34} _{-0.34}	0.12	0.28	0.87	0.68	0.21/0.07	1.62/0.96	1.63/0.96	6.05 ^{+0.13} _{-0.13}
NGC 5005	SABb	14.11 ^{+0.35} _{-0.35}	13.12 ^{+0.35} _{-0.35}	9.17 ^{+0.33} _{-0.33}	0.06	0.15	0.88	0.69	0.24/0.07	1.44/0.81	1.45/0.81	8.27 ^{+0.23} _{-0.23}
NGC 5018	E3	18.07 ^{+0.63} _{-0.63}	15.32 ^{+0.25} _{-0.25}	10.28 ^{+0.27} _{-0.27}	0.83	0.88	—	—	0.02/—	0.79/—	0.80/—	8.02 ^{+0.08} _{-0.08}
NGC 5055	Sbc	11.89 ^{+0.36} _{-0.36}	11.23 ^{+0.36} _{-0.36}	7.97 ^{+0.34} _{-0.34}	0.03	0.17	0.97	0.81	0.19/0.06	1.40/0.73	1.40/0.73	8.92 ^{+0.10} _{-0.10}
NGC 5194	SABb	10.60 ^{+0.35} _{-0.35}	10.04 ^{+0.34} _{-0.34}	7.49 ^{+0.32} _{-0.32}	—	0.10	0.87	0.88	0.17/0.06	—/0.83	—/0.83	5.96 ^{+0.36} _{-0.36}
NGC 5248	SBb	12.86 ^{+0.35} _{-0.35}	12.43 ^{+0.36} _{-0.36}	9.65 ^{+0.33} _{-0.33}	0.05	0.20	0.95	0.80	0.14/0.05	1.37/0.69	1.37/0.69	6.30 ^{+0.38} _{-0.38}
NGC 5273	S0	17.46 ^{+0.36} _{-0.36}	15.77 ^{+0.36} _{-0.36}	11.24 ^{+0.34} _{-0.34}	—	0.09	0.99	0.91	0.11/0.04	—/0.53	—/0.53	6.61 ^{+0.27} _{-0.27}
NGC 5347	SBab	15.27 ^{+0.37} _{-0.37}	14.89 ^{+0.38} _{-0.38}	11.99 ^{+0.34} _{-0.34}	0.17	0.33	0.80	0.59	0.13/0.05	1.31/0.64	1.32/0.64	7.21 ^{+0.42} _{-7.21}
NGC 5427	SABc	13.59 ^{+0.37} _{-0.37}	13.04 ^{+0.37} _{-0.37}	10.99 ^{+0.35} _{-0.35}	—	0.10	0.90	0.90	0.12/0.05	—/0.68	—/0.69	7.58 ^{+0.30} _{-7.58}
NGC 5457	SABc	9.65 ^{+0.64} _{-0.64}	9.43 ^{+0.63} _{-0.63}	7.76 ^{+0.61} _{-0.61}	—	0.05	0.95	0.95	0.11/0.04	—/0.53	—/0.53	6.41 ^{+0.08} _{-6.41}
NGC 5576	E3	17.35 ^{+0.26} _{-0.26}	15.43 ^{+0.24} _{-0.24}	10.42 ^{+0.23} _{-0.23}	0.69	0.74	—	—	0.01/—	0.25/—	0.26/—	8.44 ^{+0.13} _{-0.13}
NGC 5728	SBa	14.75 ^{+0.40} _{-0.40}	14.20 ^{+0.38} _{-0.38}	10.99 ^{+0.38} _{-0.38}	0.12	0.26	0.72	0.39	0.20/0.07	2.09/1.41	2.10/1.42	8.05 ^{+0.29} _{-0.29}
NGC 5846	E0-1	16.24 ^{+0.26} _{-0.26}	15.18 ^{+0.25} _{-0.25}	9.46 ^{+0.21} _{-0.21}	0.60	0.65	—	—	0.01/—	0.46/—	0.46/—	9.04 ^{+0.06} _{-0.06}
NGC 5879	SBbc	13.14 ^{+0.35} _{-0.35}	12.79 ^{+0.35} _{-0.35}	10.93 ^{+0.34} _{-0.34}	0.16	0.46	0.83	0.51	0.44/0.16	1.67/1.33	1.67/1.33	6.62 ^{+0.28} _{-6.62}
NGC 5921	SBbc	13.23 ^{+0.37} _{-0.37}	12.76 ^{+0.37} _{-0.37}	10.80 ^{+0.35} _{-0.35}	0.01	0.11	0.99	0.83	0.13/0.05	1.45/0.78	1.45/0.79	7.07 ^{+0.42} _{-7.07}
NGC 7418	SBc	13.35 ^{+0.37} _{-0.37}	12.94 ^{+0.35} _{-0.35}	10.82 ^{+0.33} _{-0.33}	—	0.02	0.97	0.97	0.13/0.04	—/0.61	—/0.61	5.18 ^{+1.78} _{-5.18}
NGC 7582	SBab	14.48 ^{+0.36} _{-0.36}	13.57 ^{+0.36} _{-0.36}	9.97 ^{+0.34} _{-0.34}	0.10	0.25	0.78	0.45	0.29/0.09	1.51/0.93	1.51/0.93	7.74 ^{+0.20} _{-0.20}

Table 5 continued.

TABLE 6
(Continued)

Galaxy	Type	M_{BH} (FUV)	M_{BH} (NUV)	Galaxy	Type	M_{BH} (FUV)	M_{BH} (NUV)	Galaxy	Type	M_{BH} (FUV)	M_{BH} (NUV)	Galaxy	Type	M_{BH} (FUV)	M_{BH} (NUV)	Galaxy	Type	M_{BH} (FUV)	M_{BH} (NUV)
(1)	(2)	(3)	(4)	(1)	(2)	(3)	(4)	(1)	(2)	(3)	(4)	(1)	(2)	(3)	(4)	(1)	(2)	(3)	(4)
NGC5014	1.4	7.66	7.76	NGC5448	1.4	7.66	8.02	NGC5789	7.8	4.35	3.92	NGC7059	5.6	6.25	6.04	NGC7750	5.5	6.61	6.74
NGC5016	4.4	6.52	6.60	NGC5464	9.5	4.92	4.30	NGC5798	9.7	5.24	5.01	NGC7064	5.1	4.66	4.26	NGC7755	5.0	6.77	6.90
NGC5033	5.1	7.52	8.02	NGC5468	6.0	5.52	5.32	NGC5806	3.2	8.25	8.49	NGC7070	6.0	6.12	6.10	NGC7757	5.3	5.52	5.39
NGC5042	5.0	5.91	5.46	NGC5472	2.1	8.45	8.60	NGC5809	0.2	7.14	7.13	NGC7079	-1.8	8.55	8.30	NGC7764	9.4	5.20	4.96
NGC5054	4.2	7.88	8.06	NGC5473	-2.7	9.74	9.31	NGC5821	5.0	6.96	7.25	NGC7091	7.9	4.81	4.53	NGC7793	7.4	5.67	5.64
NGC5085	5.0	7.29	7.48	NGC5474	6.1	5.17	5.34	NGC5832	3.3	5.99	5.86	NGC7107	8.6	5.60	5.46	NGC7798	5.1	6.88	6.95
NGC5101	0.2	8.41	8.30	NGC5476	7.8	6.35	6.30	NGC5850	3.1	7.84	8.31	NGC7151	5.9	6.16	6.13	PGC002492	2.0	5.27	5.40
NGC5105	5.0	5.72	5.57	NGC5477	8.8	4.24	3.95	NGC5854	-1.1	8.93	8.02	NGC7154	9.5	5.63	5.40	PGC002689	8.8	4.33	3.95
NGC5107	6.6	5.23	4.93	NGC5486	8.7	5.02	4.67	NGC5861	5.0	6.95	7.06	NGC7162	4.8	6.43	6.60	PGC003062	6.8	5.43	5.03
NGC5109	5.3	5.58	5.40	NGC5496	6.5	5.36	4.90	NGC5866B	7.9	5.86	5.69	NGC7162A	8.9	5.20	5.07	PGC003853	7.0	6.67	6.16
NGC5116	4.9	7.60	7.88	NGC5507	-2.3	8.41	9.19	NGC5878	3.2	7.76	7.76	NGC7167	5.1	5.89	5.81	PGC003855	8.8	7.90	5.33
NGC5117	5.7	5.76	5.73	NGC5520	3.1	6.99	6.97	NGC5892	7.0	5.69	5.46	NGC7184	4.5	8.02	8.45	PGC004143	9.8	5.13	4.85
NGC5134	2.9	7.85	8.13	NGC5523	5.8	6.30	6.28	NGC5915	2.7	5.60	5.14	NGC7188	3.5	6.89	7.02	PGC005329	8.0	5.38	4.99
NGC5147	7.9	5.57	5.43	NGC5534	2.1	5.98	5.97	NGC5916A	5.0	6.04	6.05	NGC7191	5.1	7.86	7.98	PGC006048	3.9	5.36	4.96
NGC5169	4.0	5.64	5.47	NGC5569	5.8	5.71	5.58	NGC5937	3.2	7.27	7.39	NGC7205	4.0	7.09	7.22	PGC006190	6.8	5.53	5.69
NGC5173	-4.9	4.61	5.72	NGC5577	3.8	7.09	7.24	NGC5949	4.0	7.15	7.24	NGC7218	5.6	6.13	5.98	PGC006228	8.7	5.60	5.44
NGC5204	8.9	4.63	4.30	NGC5584	6.0	5.77	5.61	NGC5951	5.2	6.61	6.55	NGC7219	0.6	7.25	7.50	PGC006244	10.0	4.79	4.46
NGC5205	3.5	6.68	6.81	NGC5585	6.9	5.01	4.77	NGC5954	6.0	6.96	6.67	NGC7241	4.0	7.16	7.58	PGC006626	9.9	4.92	4.67
NGC5216	-4.9	7.08	7.55	NGC5587	-0.1	4.42	5.80	NGC5956	5.9	6.61	6.88	NGC7247	3.1	7.40	7.50	PGC006703	3.1	5.87	5.69
NGC5236	5.0	6.91	6.46	NGC5595	4.9	6.33	6.19	NGC5957	3.0	6.63	6.85	NGC7254	2.9	5.99	5.83	PGC006706	9.0	5.91	5.84
NGC5238	8.0	5.04	4.83	NGC5597	6.0	6.44	6.34	NGC5962	5.1	7.01	7.08	NGC7290	4.0	5.89	5.84	PGC006864	6.9	5.26	4.82
NGC5240	5.8	6.96	7.10	NGC5600	4.8	6.61	6.44	NGC5963	4.1	5.72	5.61	NGC7314	4.0	6.98	7.21	PGC007109	9.0	6.54	7.06
NGC5247	4.1	6.59	6.46	NGC5604	1.3	6.92	7.26	NGC5964	6.9	6.08	5.93	NGC7361	4.6	5.75	5.70	PGC007654	9.9	4.97	4.79
NGC5253	8.9	5.67	5.28	NGC5608	9.8	5.15	5.01	NGC5984	6.4	6.94	6.84	NGC7371	0.0	7.15	7.33	PGC007682	1.0	5.94	5.72
NGC5254	5.0	7.26	7.64	NGC5630	7.9	5.56	5.25	NGC5985	3.0	7.63	7.94	NGC7378	2.2	7.63	7.86	PGC007900	9.0	4.42	4.01
NGC5264	9.7	6.30	6.06	NGC5631	-1.9	9.35	9.00	NGC6012	1.7	6.90	6.70	NGC7412	3.2	6.57	6.67	PGC007998	9.0	3.92	3.48
NGC5289	2.0	7.96	8.53	NGC5636	-0.4	4.80	5.18	NGC6014	-1.8	5.42	6.36	NGC7418A	6.5	4.05	3.66	PGC008295	5.0	5.00	4.68
NGC5297	4.9	6.89	7.10	NGC5645	6.6	5.95	5.72	NGC6015	5.9	6.41	6.55	NGC7421	3.7	6.97	7.19	PGC009272	8.0	5.10	4.89
NGC5300	5.2	6.37	6.55	NGC5660	5.2	5.96	5.81	NGC6063	5.9	6.68	6.73	NGC7456	6.0	5.90	5.86	PGC009354	5.1	4.50	4.14
NGC5301	4.7	7.79	7.93	NGC5661	3.2	5.63	5.50	NGC6070	6.0	6.78	6.68	NGC7462	3.6	5.77	5.54	PGC009559	7.8	5.10	4.67
NGC5304	-3.2	7.10	7.55	NGC5665	5.0	7.08	7.04	NGC6106	5.3	6.30	6.13	NGC7479	4.3	7.33	7.37	PGC010813	5.0	4.07	3.55
NGC5311	-0.1	7.43	8.00	NGC5667	6.0	5.47	5.29	NGC6140	5.6	5.40	5.22	NGC7531	4.0	6.74	7.02	PGC011367	6.9	6.19	6.02
NGC5313	3.1	8.04	8.37	NGC5668	6.9	5.26	5.01	NGC6155	5.2	6.94	6.90	NGC7590	4.4	7.01	7.19	PGC011677	9.1	5.47	5.29
NGC5320	5.2	6.46	6.59	NGC5669	6.0	5.44	5.24	NGC6168	8.0	7.16	7.77	NGC7599	5.2	7.01	7.17	PGC011744	1.0	4.34	4.05
NGC5334	5.2	6.13	6.09	NGC5691	1.2	6.37	6.26	NGC6181	5.2	7.32	7.44	NGC7661	5.9	5.44	5.29	PGC012068	10.0	4.53	4.20
NGC5336	5.9	5.44	5.43	NGC5693	6.9	6.03	5.90	NGC6236	5.9	5.27	4.85	NGC7667	8.6	3.97	3.50	PGC012439	6.2	8.22	8.22
NGC5337	2.0	8.10	8.44	NGC5701	-0.4	4.42	6.03	NGC6237	6.4	4.94	4.49	NGC7689	5.9	5.72	5.72	PGC012633	2.3	6.47	6.63
NGC5338	-2.0	4.89	4.96	NGC5708	7.8	6.41	6.42	NGC6239	3.3	5.87	5.76	NGC7690	2.9	6.79	7.02	PGC012664	6.7	5.12	4.97
NGC5339	1.1	7.03	7.17	NGC5713	4.0	7.72	7.62	NGC6255	5.9	4.54	4.17	NGC7694	10.0	6.29	6.09	PGC012981	8.7	4.87	4.86
NGC5346	5.8	6.55	6.56	NGC5714	5.8	7.71	8.15	NGC6267	4.8	6.82	6.77	NGC7714	3.1	5.85	5.84	PGC013716	4.0	7.22	7.35
NGC5350	3.6	7.16	7.24	NGC5729	3.2	6.74	6.95	NGC6339	6.3	6.53	6.16	NGC7715	9.6	5.12	4.38	PGC013821	8.9	7.68	7.59
NGC5353	-2.0	9.81	7.65	NGC5730	9.5	6.61	6.81	NGC6395	5.8	5.94	5.69	NGC7716	3.0	6.98	7.29	PGC014487	7.9	4.92	4.78
NGC5360	0.1	7.71	7.57	NGC5731	3.6	5.75	5.47	NGC6412	5.2	6.07	5.97	NGC7721	4.9	6.95	7.15	PGC016090	9.0	4.79	4.24
NGC5362	3.4	7.06	7.15	NGC5744	0.5	5.91	5.39	NGC6861E	2.0	7.00	6.97	NGC7723	3.1	7.37	7.48	PGC024469	4.2	6.50	6.28
NGC5371	4.0	7.43	7.62	NGC5757	3.1	7.13	7.04	NGC6887	3.7	7.67	7.91	NGC7724	3.1	7.50	7.66	PGC027747	6.1	5.51	5.10
NGC5375	2.4	7.16	7.53	NGC5762	2.0	5.80	5.79	NGC6889	3.7	6.24	6.09	NGC7731	1.0	6.78	7.29	PGC027825	7.0	5.24	4.82
NGC5383	3.1	7.64	7.77	NGC5768	5.3	5.99	5.91	NGC6902	2.3	6.52	6.46	NGC7732	6.7	5.92	5.86	PGC027833	7.4	5.53	5.35
NGC5425	6.5	6.24	6.19	NGC5774	6.9	5.38	5.11	NGC6902B	5.5	5.16	4.78	NGC7741	5.9	5.72	5.50	PGC029300	-1.9	7.71	7.28
NGC5426	5.0	6.65	6.64	NGC5781	2.8	7.37	7.47	NGC6925	4.0	7.28	7.44	NGC7742	2.8	7.15	7.43	PGC029653	9.9	4.25	3.90
NGC5430	3.1	7.39	7.66	NGC5783	5.2	6.03	5.98	NGC7051	0.9	7.17	7.77	NGC7743	-0.9	8.81	7.89	PGC031979	6.7	4.40	3.97

Table 6 continued.

Black hole mass—color correlation

TABLE 6
(Continued)

Galaxy	Type	M_{BH} (FUV)	M_{BH} (NUV)	Galaxy	Type	M_{BH} (FUV)	M_{BH} (NUV)	Galaxy	Type	M_{BH} (FUV)	M_{BH} (NUV)	Galaxy	Type	M_{BH} (FUV)	M_{BH} (NUV)	Galaxy	Type	M_{BH} (FUV)	M_{BH} (NUV)
(1)	(2)	(3)	(4)	(1)	(2)	(3)	(4)	(1)	(2)	(3)	(4)	(1)	(2)	(3)	(4)	(1)	(2)	(3)	(4)
PGC032091	7.0	5.74	5.82	PGC066559	8.0	4.77	4.17	UGC04305	9.9	3.85	3.39	UGC05522	6.4	4.47	4.01	UGC06399	8.8	5.77	5.73
PGC035271	7.0	4.47	3.83	PGC067871	7.0	4.74	4.32	UGC04390	6.6	5.56	5.47	UGC05540	5.9	5.40	4.90	UGC06433	9.2	4.83	4.45
PGC035705	7.9	4.89	4.48	PGC068061	0.1	6.02	5.86	UGC04426	9.8	5.01	4.53	UGC05571	8.8	4.21	3.58	UGC06446	6.6	4.18	3.83
PGC036274	9.0	5.72	5.41	PGC068771	6.6	5.42	5.24	UGC04499	8.0	4.53	4.14	UGC05612	8.0	5.87	5.79	UGC06512	5.3	4.63	4.30
PGC036551	7.6	5.44	5.14	PGC069114	6.9	4.93	4.50	UGC04514	5.9	5.28	5.08	UGC05642	4.1	6.75	6.67	UGC06517	3.8	6.09	6.02
PGC036643	6.3	5.16	4.89	PGC069224	9.8	4.43	4.23	UGC04543	7.9	4.23	3.77	UGC05646	4.0	5.94	5.81	UGC06526	7.0	6.68	6.57
PGC037238	8.0	4.31	3.87	PGC069293	8.9	5.65	5.57	UGC04549	8.1	6.43	6.96	UGC05676	8.0	5.81	5.73	UGC06534	6.4	5.53	5.24
PGC037373	5.8	5.00	4.74	PGC069339	9.9	4.30	4.52	UGC04550	3.4	7.68	7.55	UGC05677	8.0	5.01	4.43	UGC06570	-0.2	5.10	5.47
PGC039799	9.1	4.50	3.95	PGC069404	8.0	7.10	7.42	UGC04628	5.8	5.96	5.73	UGC05688	8.8	5.24	4.99	UGC06575	5.8	5.36	5.40
PGC040408	8.9	5.60	5.40	PGC069448	4.0	6.34	6.33	UGC04659	8.0	5.49	5.17	UGC05707	5.9	4.97	4.78	UGC06603	5.9	5.41	5.14
PGC040447	10.0	5.07	4.57	PGC072006	9.0	4.90	4.57	UGC04701	7.0	5.82	5.65	UGC05720	9.9	5.68	5.50	UGC06628	8.8	4.97	4.67
PGC040552	5.4	7.85	7.95	PGC072252	5.0	4.60	4.27	UGC04704	7.9	4.75	4.31	UGC05739	9.7	7.93	8.05	UGC06713	8.6	5.16	4.86
PGC041743	9.0	6.30	6.17	PGC091215	7.9	5.54	5.40	UGC04714	3.1	6.80	6.85	UGC05740	8.8	4.83	4.55	UGC06782	9.8	5.38	5.03
PGC041965	8.0	5.56	5.48	PGC091228	7.9	5.13	4.49	UGC04722	7.9	3.90	3.28	UGC05764	9.9	3.69	3.18	UGC06791	6.5	7.18	7.29
PGC042068	3.1	6.96	6.77	PGC091413	7.9	5.43	4.79	UGC04777	9.2	5.77	5.51	UGC05791	3.0	4.79	4.34	UGC06816	9.9	4.60	4.23
PGC042160	9.5	4.83	4.55	PGC1059326	3.6	4.32	3.95	UGC04787	7.9	5.28	4.96	UGC05798	6.4	4.96	4.50	UGC06840	8.8	5.34	5.48
PGC042868	8.0	5.51	5.77	UGC00017	9.1	5.67	5.59	UGC04797	8.8	6.06	5.69	UGC05829	9.8	3.88	3.34	UGC06849	8.8	5.39	5.18
PGC043236	7.6	5.89	5.65	UGC00132	7.9	6.34	6.15	UGC04800	5.9	6.30	6.28	UGC05832	4.2	5.36	4.99	UGC06862	6.7	6.24	5.84
PGC043341	10.0	4.84	4.46	UGC00156	9.8	6.12	5.37	UGC04834	8.0	5.38	5.28	UGC05833	-2.0	2.83	4.01	UGC06879	7.1	6.60	6.66
PGC043345	9.0	5.06	4.72	UGC00313	4.3	6.52	6.49	UGC04837	8.7	5.27	4.92	UGC05844	6.6	6.10	6.02	UGC06900	9.7	6.72	6.41
PGC043458	9.0	5.34	5.07	UGC00634	8.8	4.86	4.53	UGC04841	6.9	5.51	5.40	UGC05846	9.9	4.42	4.03	UGC06903	5.9	5.94	6.02
PGC043679	6.5	6.93	6.81	UGC00711	6.5	5.64	5.32	UGC04845	6.9	6.31	6.08	UGC05897	5.2	6.60	6.62	UGC06917	8.8	5.67	5.46
PGC043851	9.8	4.24	3.68	UGC00866	7.8	5.52	5.30	UGC04867	7.0	4.72	4.38	UGC05918	9.8	4.39	3.87	UGC06922	3.8	5.70	5.52
PGC044157	9.0	5.70	5.61	UGC00882	9.8	5.54	5.33	UGC04871	8.8	4.76	4.28	UGC05921	8.1	5.82	5.41	UGC06931	9.0	4.91	4.53
PGC044278	7.9	4.59	4.20	UGC00891	9.0	5.05	4.81	UGC04953	7.0	5.16	4.96	UGC05922	6.8	5.81	5.68	UGC06955	9.8	5.27	5.00
PGC044735	9.7	4.98	4.94	UGC00941	9.9	4.75	4.42	UGC04970	5.7	7.56	7.66	UGC05934	8.0	4.91	4.53	UGC06956	8.8	5.50	5.28
PGC044906	8.0	4.69	4.12	UGC00964	3.0	6.41	6.23	UGC04982	7.9	7.05	7.11	UGC05947	10.0	4.62	4.26	UGC07009	9.9	4.91	4.49
PGC044952	5.0	6.32	6.02	UGC01014	9.3	5.19	4.81	UGC04988	9.0	5.90	5.81	UGC05979	9.9	4.85	4.27	UGC07019	9.9	5.41	5.06
PGC044954	3.0	5.44	5.11	UGC01020	2.1	8.13	7.75	UGC05004	10.0	6.69	6.70	UGC05989	9.9	4.99	4.61	UGC07035	1.0	5.94	5.69
PGC044982	9.7	5.24	4.42	UGC01104	9.5	5.00	4.74	UGC05015	7.9	5.99	5.93	UGC05990	2.0	7.06	7.36	UGC07053	9.9	4.73	4.31
PGC045195	7.7	4.46	3.99	UGC01110	5.9	6.38	6.55	UGC05107	6.4	5.09	4.79	UGC06014	8.0	5.35	4.97	UGC07089	7.9	6.10	5.91
PGC045257	9.0	4.95	4.59	UGC01112	5.8	6.20	6.06	UGC05114	9.9	4.69	4.28	UGC06023	6.6	6.16	6.08	UGC07094	8.0	7.22	6.79
PGC045359	9.9	4.20	3.45	UGC01176	9.9	4.75	4.26	UGC05179	3.7	6.89	6.31	UGC06083	4.1	6.27	6.30	UGC07129	2.0	8.24	8.28
PGC045652	6.7	6.67	6.50	UGC01195	9.8	5.12	4.72	UGC05228	4.9	7.00	6.70	UGC06104	4.0	5.44	5.06	UGC07133	6.6	5.82	5.61
PGC045824	6.7	4.55	4.82	UGC01197	9.8	5.46	5.15	UGC05238	7.0	6.63	5.79	UGC06112	7.4	5.17	4.89	UGC07143	4.9	5.44	5.22
PGC045877	4.9	8.04	8.19	UGC01200	9.9	5.36	5.15	UGC05249	6.7	5.19	4.78	UGC06145	9.9	5.33	4.93	UGC07153	5.9	6.33	6.19
PGC046382	9.9	5.49	5.11	UGC01240	7.9	4.78	4.34	UGC05349	7.8	5.17	4.89	UGC06151	8.8	4.87	4.50	UGC07175	7.8	4.67	3.92
PGC047721	4.0	8.31	8.62	UGC01547	9.9	4.23	3.90	UGC05354	4.3	4.40	3.95	UGC06157	7.8	4.91	4.60	UGC07184	6.4	5.66	5.44
PGC047846	8.9	6.26	6.39	UGC01551	6.1	5.52	5.47	UGC05358	3.1	5.45	5.25	UGC06162	6.4	5.20	4.97	UGC07218	9.9	5.09	4.81
PGC048087	8.0	6.09	5.28	UGC01670	8.8	4.86	4.57	UGC05373	9.9	5.08	4.77	UGC06169	3.0	6.97	7.06	UGC07239	9.8	6.04	5.97
PGC050229	1.1	5.52	5.33	UGC01862	6.4	6.50	6.52	UGC05391	8.9	4.33	3.83	UGC06171	9.9	4.88	4.61	UGC07249	9.5	4.97	4.57
PGC051291	2.0	4.91	4.52	UGC01981	9.7	6.52	6.37	UGC05393	8.0	4.65	4.84	UGC06181	9.7	4.68	4.23	UGC07257	8.1	4.49	4.56
PGC051523	9.0	4.54	4.17	UGC02275	8.8	3.92	3.29	UGC05401	9.7	5.30	4.86	UGC06194	4.9	5.45	5.10	UGC07267	7.8	5.32	4.88
PGC052940	9.9	4.16	3.44	UGC02345	8.8	4.70	4.26	UGC05423	9.9	5.49	5.18	UGC06249	5.9	5.12	4.93	UGC07271	6.9	5.60	5.30
PGC053134	8.0	4.70	4.30	UGC02429	9.0	5.47	5.36	UGC05427	7.7	4.89	4.46	UGC06271	1.0	7.81	8.15	UGC07300	9.8	4.65	4.34
PGC053568	8.0	4.95	4.56	UGC04024	5.8	6.18	6.05	UGC05446	5.9	4.96	4.67	UGC06309	4.5	7.11	7.19	UGC07332	9.9	4.29	3.79
PGC053764	5.5	6.54	6.38	UGC04121	8.8	5.26	5.04	UGC05451	9.9	6.25	6.10	UGC06320	8.0	5.64	5.30	UGC07396	7.6	5.71	5.32
PGC054944	1.8	6.28	6.09	UGC04148	7.2	4.37	3.95	UGC05456	9.0	4.68	4.13	UGC06335	6.0	5.33	5.37	UGC07408	9.8	5.67	5.14
PGC065367	9.9	5.02	3.95	UGC04151	7.9	6.01	5.91	UGC05464	8.7	5.18	4.90	UGC06345	9.9	4.47	3.77	UGC07557	8.8	4.30	4.40
PGC066242	4.1	5.56	5.29	UGC04169	5.8	5.30	5.06	UGC05478	9.9	5.23	5.03	UGC06378	6.5	5.44	5.03	UGC07559	9.9	4.34	3.94

Table 6 continued.

TABLE 6
(Continued)

Galaxy	Type	M_{BH} (FUV)	M_{BH} (NUV)	Galaxy	Type	M_{BH} (FUV)	M_{BH} (NUV)	Galaxy	Type	M_{BH} (FUV)	M_{BH} (NUV)
(1)	(2)	(3)	(4)	(1)	(2)	(3)	(4)	(1)	(2)	(3)	(4)
UGC07577	9.8	5.51	5.15	UGC08614	9.9	6.28	6.08	UGC09837	5.3	5.33	5.24
UGC07590	4.1	4.86	4.50	UGC08629	9.8	6.18	6.28	UGC09858	4.0	6.61	6.59
UGC07596	9.8	7.14	6.66	UGC08630	5.7	5.85	5.69	UGC09875	8.9	5.58	5.46
UGC07599	8.7	4.29	3.86	UGC08639	9.7	5.47	5.19	UGC09936	8.8	4.88	4.67
UGC07605	9.9	4.33	3.88	UGC08642	6.8	4.89	4.59	UGC09951	6.6	4.99	4.56
UGC07612	8.8	4.84	4.53	UGC08651	9.9	4.14	3.59	UGC09977	5.3	6.89	7.39
UGC07639	9.9	5.79	5.32	UGC08658	5.0	5.94	5.93	UGC09979	9.9	4.86	4.68
UGC07673	9.9	4.93	4.68	UGC08684	5.9	8.22	8.37	UGC09992	9.9	4.85	4.30
UGC07690	9.9	4.88	4.31	UGC08688	7.8	4.69	4.38	UGC10020	6.6	5.46	5.35
UGC07698	9.9	4.97	4.67	UGC08693	4.2	6.95	7.18	UGC10054	8.0	5.28	5.00
UGC07699	6.1	5.23	4.86	UGC08733	5.9	5.15	4.92	UGC10061	9.9	4.76	4.14
UGC07700	7.9	4.91	4.56	UGC08760	9.8	4.65	4.14	UGC10290	8.8	4.67	4.30
UGC07719	8.0	4.76	4.31	UGC08795	6.0	6.15	6.05	UGC10413	5.7	6.05	6.15
UGC07730	8.8	5.59	5.24	UGC08839	9.9	4.86	4.28	UGC10445	6.0	5.01	4.63
UGC07739	9.8	6.11	5.83	UGC08851	7.9	4.84	4.43	UGC10608	8.0	3.58	3.15
UGC07774	6.3	5.82	5.41	UGC08877	8.0	5.44	5.51	UGC10721	5.8	6.82	6.68
UGC07795	9.8	3.92	3.52	UGC08892	9.9	4.89	4.59	UGC10736	8.0	4.85	4.23
UGC07802	6.1	6.58	6.45	UGC08909	6.9	5.73	5.83	UGC10791	8.8	6.44	6.39
UGC07824	9.0	6.13	6.05	UGC08995	7.4	5.63	5.40	UGC10806	8.0	4.37	4.43
UGC07844	6.1	7.12	7.14	UGC09057	7.0	4.53	4.24	UGC10854	6.0	5.11	5.20
UGC07906	9.9	4.62	4.26	UGC09071	5.9	6.10	5.97	UGC11782	8.8	4.98	4.61
UGC07911	8.8	5.32	5.21	UGC09126	9.8	4.96	4.66	UGC12151	9.7	5.24	5.08
UGC07941	7.0	4.90	4.56	UGC09128	9.9	4.71	4.14	UGC12178	8.0	5.27	4.72
UGC08041	6.9	5.74	5.61	UGC09206	3.8	5.93	5.59	UGC12613	9.8	6.06	5.19
UGC08048	9.5	5.09	4.64	UGC09215	6.3	5.21	4.90	UGC12681	4.2	4.35	3.91
UGC08052	4.7	6.79	6.82	UGC09240	9.9	4.87	4.41	UGC12682	9.8	4.62	4.09
UGC08053	8.0	4.49	4.02	UGC09242	6.6	5.32	4.93	UGC12709	8.7	5.36	5.25
UGC08056	6.4	4.74	4.42	UGC09274	4.2	5.98	5.93	UGC12732	8.7	4.42	4.02
UGC08084	8.0	5.49	5.08	UGC09299	6.4	4.50	4.06	UGC12791	9.9	5.15	4.79
UGC08127	9.8	4.98	4.63	UGC09310	8.0	5.87	5.55	UGC12843	8.2	4.94	4.56
UGC08146	6.4	5.05	4.64	UGC09356	4.6	5.70	5.51	UGC12846	8.7	4.92	4.59
UGC08153	6.6	4.89	4.59	UGC09364	7.8	5.42	5.21	UGC12856	9.6	4.48	4.59
UGC08155	2.2	6.58	6.75	UGC09380	9.9	4.46	4.16				
UGC08181	8.0	5.32	5.19	UGC09389	3.2	5.47	5.12				
UGC08201	9.9	4.25	3.79	UGC09392	10.0	5.29	4.95				
UGC08246	5.9	4.61	4.28	UGC09394	5.9	4.85	4.53				
UGC08282	5.9	5.37	4.71	UGC09448	3.3	8.17	8.34				
UGC08303	9.9	4.51	4.17	UGC09469	9.7	5.43	5.18				
UGC08313	5.0	5.67	5.39	UGC09470	7.9	4.91	4.55				
UGC08320	9.9	4.49	3.98	UGC09482	6.6	5.60	5.07				
UGC08331	9.9	4.72	4.26	UGC09569	6.6	4.64	4.19				
UGC08365	6.4	5.26	5.01	UGC09601	5.9	5.41	5.24				
UGC08385	9.0	4.95	4.61	UGC09661	8.0	6.05	5.97				
UGC08441	9.9	4.92	4.74	UGC09663	9.8	4.92	4.63				
UGC08449	7.9	4.88	4.70	UGC09682	8.6	5.30	4.79				
UGC08489	8.0	4.31	3.92	UGC09730	6.6	5.07	4.68				
UGC08507	9.8	5.33	5.18	UGC09746	4.0	7.09	7.07				
UGC08516	5.9	5.78	5.62	UGC09760	6.6	4.82	4.23				
UGC08588	8.8	5.23	5.08	UGC09815	7.9	5.34	5.29				
UGC08597	6.6	4.96	4.89	UGC09816	9.8	5.65	5.50				

Table 6 continued.